PROPAGATION OF MECHANICAL STRAIN IN PERIPHERAL NERVE TRUNKS AND THEIR INTERACTION WITH EPINEURAL STRUCTURES

A Thesis

Submitted to the Faculty

of

Purdue University

by

T.G. Hunter Cox

In Partial Fulfillment of the

Requirements for the Degree

of

Master of Science in Biomedical Engineering

August 2017

Purdue University

Indianapolis, Indiana

THE PURDUE UNIVERSITY GRADUATE SCHOOL
STATEMENT OF COMMITTEE APPROVAL

Dr. Ken Yoshida, Chair

Department of Biomedical Engineering

Dr. John Schild

Department of Biomedical Engineering

Dr. Joseph Wallace

Department of Biomedical Engineering

Approved by:

Dr. Julie Ji

Head of the Graduate Program

I would like to dedicate this thesis and work to my son and to my wife, Madisen.

Without your support this work would not have been accomplished.

ACKNOWLEDGMENTS

I would like to thank Dr. Yoshida for his guidance in this work and for providing me with the right challenges I needed to grow as an engineer and a scholar. My exposure to his work and the work of others in the growing field of neural engineering is eye opening and inspiring.

I would also like to thank the professors I have had at IUPUI who have provided me with guidance in my time and provided me with information that was critical to my work on this thesis and as a member of society: Dr. Karen Alfrey, Dr. Edward Berbari, Dr. Sungsoo Na, Dr. John Schild, Dr. Terri Talbert-Hatch, Dr. Joseph Wallace, Carol Bain, and Sherry Clemens.

I want to thank my colleagues: Chandrama Ahmed, Michael Bertram, Caleb Comoglio, and Ryne Horn for all of the help they have provided with experiments, homework, input on writing, and support through troubling times. I would also like to thank individuals I have worked with on the PLTL project: Zachary Bart, Ian Daly, Kyle McElyea, Brittany Frecker, Brian Frondorf, David Kane, Katelyn Thuman, and Grant Wible.

I would like to acknowledge the IUPUI Biomedical Engineering Department for helping make the fulfillment of this degree possible through providing a Research Assistantship with which I was able to attend graduate school. I would also like to thank Glaxo-Smith-Kline for providing the funding for all projects through their grant to Dr. Yoshida.

TABLE OF CONTENTS

Page

Page

LIST OF TABLES

LIST OF FIGURES

Figure Page

LIST OF SYMBOLS

ε	strain
$m\varepsilon$	millistrain
E_{reci}	reciprocal electric field
F	force
i_m	transmembrane current density
I_r	unit reciprocal current
J_i	spatial volume source
J_i'	uniform current density
J_{reci}	reciprocal current field
κ	conductivity
ξ	Spatial frequency (1/m)
S	sensitivity
σ	stress
V_e	electric potential
w	weighting function
x	displacement
Φ_{reci}	lead scalar potential field
Φ_e	extracellular potential
Z_t	transfer impedance

LIST OF ABBREVIATIONS

ANS	Autonomic Nervous System
DRG	Dorsal Root Ganglia
E	Elastic Modulus
EMG	Electromyography
FINE	Flat Interface Nerve Electrode
FEA	Finite Element Analysis
FEM	Finite Element Model
FINE	Flat Interface Nerve Electrode
FNS	Functional Neuromuscular Stimulation
GVE	General Visceral Efferent
H&E	Hematoxylin & Eosin
IU	Indiana University
LARC	Laboratory Animal Research Center
LIFE	Longitudinal Intrafascicular Electrode
mN	milliNewton
PNS	Peripheral Nervous System
SD	Standard Deviation
SELINE	Self-Opening Intraneural Peripheral Interface
SPINE	Slowly Penetrating Interfascicular Electrode
SMP	Shape Memory Polymer
SMB	Standard Mechanical Body
SSNS	Sensory-Somatic Nervous System
TIME	Transverse Intrafascicular Multichannel Electrode
VNS	Vagal Nerve Stimulation

ABSTRACT

Cox, T. G. Hunter M.S.B.M.E., Purdue University, August 2017. Propagation of Mechanical Strain in Peripheral Nerve Trunks and their Interaction with Epineural Structures. Major Professor: Ken Yoshida.

Advances in peripheral nerve electrode technology have outpaced the advances in chronic implantation reliability of the electrodes. An observable trend is the increased deposition of fibrotic encapsulation tissue around the electrode to shift its position away from the implantation site and subsequently reducing performance. A finite element model (FEM) is developed in conjunction with tensile testing and digital image correlation of strain to understand the relationship between cuff electrode attachment and the strain environment of the nerve.

A laminar and bulk nerve model are both developed with material properties found in literature and geometry found from performing histology. The introduction of a cuff electrode to an axially stretched nerve indicates a significant behavior deviation from the expected response of the axial strain environment. When implemented in ex-vivo tensile testing, results indicate that the reduction of strain is statistically significant but becomes much more apparent when paired with a digital image correlation system to compare predicted and measured effects.

A robust FEM is developed and tested to emphasize the effect that the boundary conditions and attachment methodology significantly effects the strain environment. By coupling digital image correlation with FEM, predictive models can be made to the strain environment to better design around the long term chronic health of the implant.

1. AN INTRODUCTION TO THE USE OF ELECTRODES IN THE PERIPHERAL NERVOUS SYSTEM

Current estimates predict that by the year 2050 there will be approximately 3.6 million Americans living with the amputation of a limb [1]. In day-to-day life, amputees experience loss of function, physical discomfort, lack of mobility, and phantom limb pain. The use of a prosthetic can help with regaining function and mobility for amputees, but there is a disconnect that exists in current prosthetic technology. Currently, there is almost no tactile feedback, and control of the prosthetic limb is often crude. Fine motor function is often limited, and when coupled with a lack of feedback, the prosthetic can be difficult to control and learn how to use. If a sophisticated, neurointegrated prosthetic is created with control that closely mimics the pre-amputated state it may be possible to greatly improve the quality of life of amputees. With the increase of more than double the current population of amputees predicted by 2050 [1], the need for the advancement of prosthetic technology is apparent. The problem is that long term stability of these interfaces prevents the use of modern and cutting edge electrodes. In the case of neural prostheses, the scarring of the tissue results in electrode-fiber separation and degradation of electrode performance

Currently available technology depends on the use of functional neuromuscular stimulation (FNS) to evoke activation of muscle or other end organ tissue via the use of implantable electrodes. The use of these electrodes in the peripheral nervous system covers a wide range of areas including treatment of epilepsy [2], sleep apnea [3], and control of upper-limb prostheses [4, 5].

The technical ability to cover a wide range of applications is dependent on understanding how the electrode and targeted nerve interact in the context of FNS. Different electrode designs target and seek to reach neural information through varying means of implantation location and manipulation of the nerve.

This chapter briefly reviews and discusses the anatomy of the nervous system, the design and considerations of different electrodes currently in use in FNS, and how the body interacts with the electrodes. It is necessary to discuss the anatomy of the body as it is a primary driving force in how electrodes are designed to target neural information. Current electrode designs cover a large variety of application; it is important to understand why they are designed by discussing how an electrode and nerve couple together to make a system for recording and stimulation. When designing an electrode, it is not only important to consider the acute electrical coupling, it is also important to consider the biocompatibility of the electrode. Neural integrated prosthetics require long term implantation so it is important to examine chronic studies in order to improve the chronic longevity of the implant.

While the electrode-fiber interaction is primarily an interaction of electrical effects, the interaction of the body as a whole with the nerve is a complex mechanical, chemical, electrical, and biological interaction. Yuan-Cheng Fung first described and theorized that Wolff's law had an application in all tissue that mechanical stresses and strain act as an impetus for change in geometry, composition, and remodeling of surrounding tissue [6]. It is this theory of strain effects on soft tissue that drives the fundamental hypothesis and actions of the present work.

1.1 Anatomy of the Peripheral Nervous System

The primary interest for many researchers is to interface with the peripheral nervous system (PNS), hereafter defined as the nerves and ganglia external to the spinal cord and brain. It consists of efferent and afferent nerve axons that connect with the motor organs, sensory organs, and the dorsal root ganglia (DRG) [7].

When implanting electrodes, generally the DRG are avoided and the long axons are targeted. These axonal regions of nerves consist of a well known hierarchical structure. A peripheral axon (also referred to as a nerve fiber) is surrounded by a Schwann cell if it is myelinated, which is then surrounded by a volume of connective

tissue known as the endoneurium. Multiple axons are linked with connective tissue and wrapped into a fascicle by a membrane known as the perineurium. Figure 1.1 demonstrates this hierarchical nature of the nerve. It is important to note that many nerves consist of both myelinated and unmyelinated fibers. These fascicles are linked together with connective tissue and supplied with nutrients through blood vessels and enveloped by the membrane known as the epineurium. From here, the nerve is surrounded by connective tissue, muscle, or other organs.

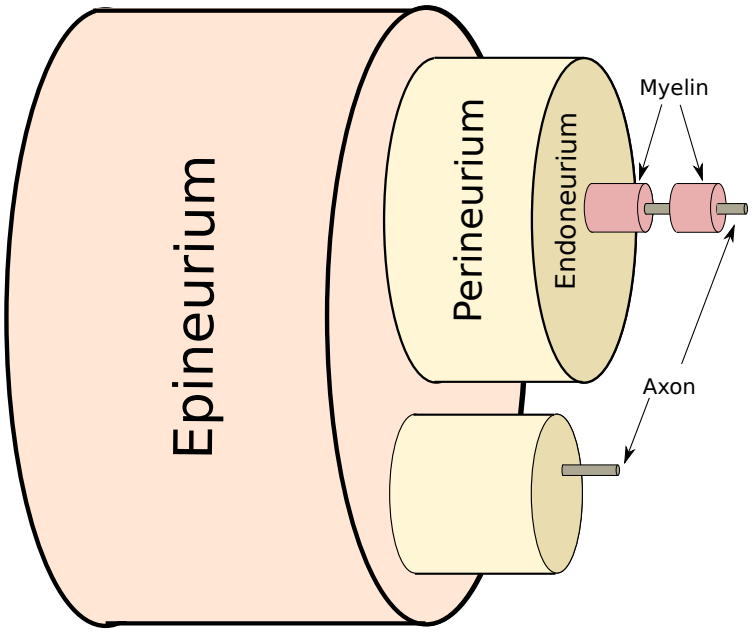

Fig. 1.1.: A simple diagram (not to scale) of a nerve demonstrating the hierarchy of axon, myelin, endoneurium, perineurium, and epineurium.

When implanting electrodes, there is much to consider about the targeted placement with respect to the anatomy. For example, one must be consider whether the electrode is targeting the entire nerve, a single fascicle, or a single fiber. It is also critically important to understand the end organ being targeted for effect.

While nerves follow the same hierarchical pattern, there is variation in size, myelination, and axonal density to create the many functions of the PNS. These many functionalities are defined by the two main sub-systems of the PNS: the Autonomic Nervous System (ANS) and the Sensory-Somatic Nervous System (SSNS).

1.1.1 The Sensory-Somatic Nervous System

The Sensory-Somatic Nervous System (SSNS) is primarily responsible for voluntary control of the skeletal muscles. It consists of efferent nerves that conduct signal to stimulate muscle contraction and afferent nerves that send signal from sensory locations such as the skin to inform the body of external stimuli. The SSNS is composed of two parts: the spinal and cranial nerves.

The spinal nerves carry sensory information into the spinal cord for primary motor function with tactile feedback from other peripheral nerves. The cranial nerves carry information to and from the brainstem.

1.1.2 The Autonomic Nervous System

The Autonomic Nervous System (ANS) is primarily responsible for the control and functionality of internal organs that act without conscious thought. It acts to regulate bodily activity such as digestion, urination, sexual arousal, heart and respiratory rate, and the fight-or-flight response. This regulation and control is through the two subsystems: the sympathetic and parasympathetic pathways [8].

The sympathetic pathway acts to control the fast acting responses of the viscera. It consists of cells with their bodies in the thorax (T1) to lumbar (L2/3) region of the lateral grey column. These preganglionic neurons extend to the General Visceral Efferent (GVE) neurons with several locations for the synapse to occur.

The parasympathetic pathway acts to control the slow response and dampen the fast response of the viscera. It consists of cells with their bodies in the the brainstem and sacral spinal cord. These neurons act to excite and inhibit activity with sensory

feedback. Of special concern for many researchers, and the nerve examined in this thesis is the tenth cranial nerve: the vagus.

The Tenth Cranial Nerve: the Vagus

The tenth cranial nerve, known commonly as the vagus, cranial nerve ten (CNX) and the pneumogastric nerve, is the primary interface of the central nervous system (CNS) in parasympathetic pathway control of the heart, lungs, and digestive tract [9]. It also acts to receive and function in a sympathetic pathway using peripheral receptors. It is the longest nerve in the ANS and is comprised of both afferent and efferent fibers to conduct information both to and from the end organ and CNS.

This highly complex nerve with bidirectional information is useful for researchers because of the wealth of information that can be potentially gained. Researchers can use the nerve to affect end organs and simultaneously record signals being conducted back to the CNS. Vagal Nerve Stimulation (VNS) has been used with a pacemaker-like device to control seizures in epilepsy patients [10], treatment of depression [11]. There is potential for many more clinically-refined uses given the known multitude of organs stimulated by the vagus.

The vagus nerve presents a complex, information-dense source of study that can be used as an example model in electrode study and refinement. To examine what information can be gained from the implantation of an electrode into a nerve, it must be discussed what the considerations are for designing an electrode and what electrodes are currently in use in the peripheral nervous system.

1.2 Review of Electrodes in the Peripheral Nervous System

To interface electronically with a nerve is to create a physical connection, much like a plug connects to an outlet. A conductive metal contact is introduced to an electrically active medium with the intention of pulling information about the activity from the medium. In the case of the peripheral nerve, there are varying methods to

introduce the contact to the medium. In addition, there are a multitude of methods to manipulate the medium to access different sets of information that are incorporated into the design. By manipulating size and geometry, fundamental design considerations can be modulated.

1.2.1 Electrode Design Considerations

Horch and Yoshida [12] describe the ideal peripheral nerve electrode as having fifteen optimized characteristic properties. Optimized *selectivity* to record and stimulate from a specified population size of units or axons. Functional *unit selectivity* to record and stimulate a singular axon without interference from other units. Discriminating *size selectivity* to determine activity based on the size of the axon or unit. *Spatial selectivity* to record from multiple specific locations along the length of a nerve. Information *reach* to determine and estimate information throughout the entirety of the nerve based on information that is known. Controlled *signal-to-noise ratio* to clarify the signal from external influence. Characterized and lowered *electrode impedance* to reduce the effects of noise and increase functional recording and stimulation. Defined *coherence and correlation* to directly infer source, destination, and effect of a signal. Minimized *invasiveness* to reduce the chance for the body to reject the electrode. Surgical speed and *ease of implantation* to simplify and minimize surgical time to reduce risks associated with surgery. Known *lifespan* of the implant to critically predict when a failure may occur to prevent any life threatening situation. *Biocompatibility* to maximize the life span and use of the electrode through material properties. *Chronic recording stability* to increase long term performance of the electrode. Increased *robustness* to prevent wear and tear of the electrode over its lifespan. Minimized *cost* to increase availability and incentivize use in prosthetic integration.

Ideally, each of these properties would be optimized for any given electrode but it is very difficult to achieve this because of conflicting design parameters. Increasing

total selectivity interferes with unit selectivity. Increasing reach and spatial selectivity requires more implantation sites and is therefore in contradiction with decreasing cost, ease of implantation, and minimized invasiveness.

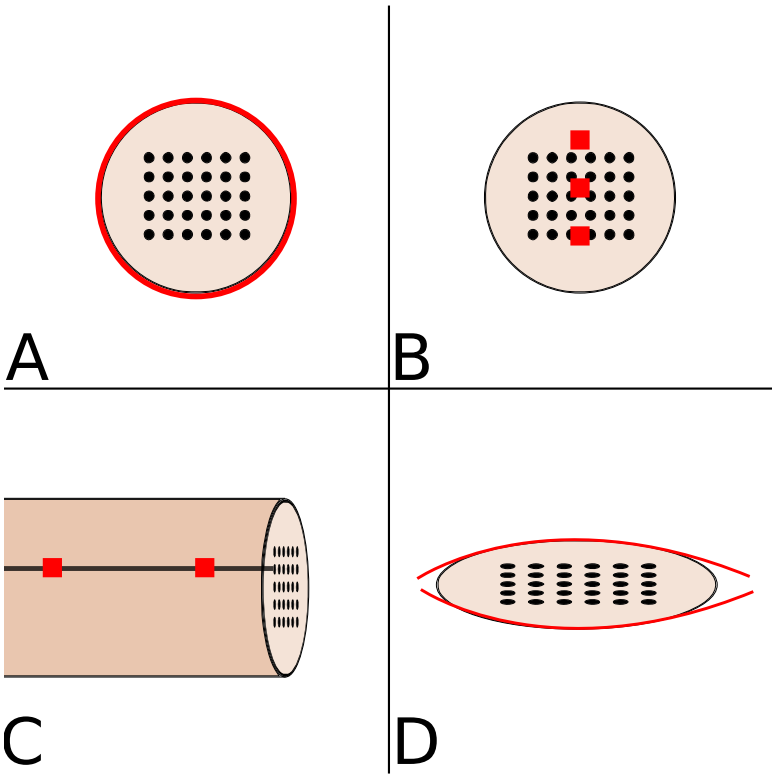

Fig. 1.2.: An illustration of methods to extract information from the nerve without true scale. Red illustrates an electrode contact, black represents an axon, and beige represents general nervous tissue. (A) illustrates an extraneural cuff design which records and stimulates whole nerve activity. (B) illustrates a transverse electrode to record and stimulate from specific unit populations. (C) illustrates a longitudinal electrode to record and simulate at different spatial points of the same axon. (D) illustrates an extraneural cuff design that compresses the nerve to increase contact with the nerve for fine-tuned control.

Much of the design consideration for an electrode comes from the desired manipulation of the media. Figure 1.2 illustrates the various orientations of electrode contact placement to target different information. Extraneural geometries attempt to record

and stimulate the entire nerve. This is achieved with a contact wrapped around the whole nerve, with some variation on how tightly fitting the electrode is to the nerve. Intrafascicular geometries can access the source of electrical potentials more directly by gaining proximity to the axons. In general, intrafascicular electrodes can be designed in arrays to access axon populations in the same section of longitudinal space of the nerve or along multiple longitudinal locations of the same axon.

With these considerations in mind, many researchers have attempted to optimize their electrode designs for varying applications for implantation in the peripheral nervous system.

1.2.2 Transverse Intrafascicular Multichannel Electrode

The origination of all intrafascicular recording electrodes comes from the concept of the microneurography needle electrode [13]. In its most basic form, an electrode recording site is located at the tip of a hypodermic needle that penetrates the perineurium and rests in the endoneural space [14].

It was noted and heavily debated whether or not the microneurography needles were capable of making the intended recordings [15], and thus the need for a multicontact array was determined. An early iteration of these Transverse Intrafascicular Multichannel Electrode (TIME) arrays were implanted and able to record electromyography (EMG) signal, but there was no evidence of neural recording [16]. However, developments in technology led to these arrays being able to record and stimulate acute cortical tissue [17], acute peripheral nerve [18, 19], acute spinal cord [20], and sub-chronic peripheral nerve [21].

The key to the success of the TIME is that, instead of searching for active units during implantation, the probability of finding an active unit in a given section is increased by the presence of multiple contacts in the same space. The use of multiple spatial implantation sites can allow for the spatial averaging technique as seen

commonly in cortical measurements [22]. However, functionally identifying and correlating recorded activity between spatially separated sites can be cumbersome.

1.2.3 Longitudinal Intrafascicular Electrode

The success of microneurography needles and TIME arrays in being able to record intrafascicular signal led to the development of the Longitudinal Intrafascicular Electrode (LIFE). While the TIME aims to record from multiple populations in the same space, the LIFE is implanted parallel to the longitudinal axis of the nerve with active sites along the length of the electrode and not at the insertion tip. This enables the structure to be pulled through entry and exit points without exposing the active sites to the external environment. This method seeks to make recordings along the length of a single fiber to understand spatial relationships.

The concept was first tested in rabbit and cat models [23] to observe potential for sub-chronic demyelination or denervation. Soon after, refined iterations of the LIFE structure were made in Utah utilizing deinsulation techniques to refine structural composition and use electrodeposition to reduce interfacial impedance and thermal noise [24]. Later, refined stimulation and recording selectivity were examined [25, 26].

Efforts continued to be made in chronic recordings using thin-film [27] and silicone [28] variations of the LIFE array with effective characterization on electrode spacing EMG/stimulus artifact rejection. This was confirmed in a sub-chronic human model with highly selective recording and stimulation [29].

1.2.4 Self-Opening Intraneural Peripheral Interface

While both the TIME and LIFE structures succeed with their intended effects, there was a chronic risk for electrode displacement with muscular movement or displacement by scar tissue. This displacement renders the electrode unable to function. Micera and Navarro [30] attempted to solve this problem with the implementation of the Self-Opening Intraneural Peripheral Interface (SELINE).

The design of the SELINE creates an active wing array that uses tines to mechanically stabilize itself. The designers found that the SELINE requires ten to fifteen times more force than a TIME or a LIFE to remove from a peripheral nerve.
Acute studies showed that there was sufficient selectivity in recording and stimulating but further chronic analysis needs to be performed.

1.2.5 Cuff Electrodes

While the TIME, LIFE, and SELINE arrays focus on the intraneural signal, there exists the extraneural class of electrodes. The circumferential cuff electrode is one of the most commonly used and studied electrodes in many applications because of their low invasiveness. The first cuff electrode used for chronic recording was designed with cutaneous and muscle afferent targets [31, 32]. This electrode was cut down the long axis and fit around the nerve to create an insulating seal. While this makes an insulating current [33], it is a necessary step to prevent from cutting the nerve directly to fit into a cuff.

Iterations of the cuff have been made to address this leak current with piano hinge designs [28], overlapping flaps [33], and self-spiraling cuffs [34, 35]. With these electrical improvements, geometric size and surgical implantation complexity increase making a simple design increasingly difficult to use. While trying to limit electrical leak, surgical performance is crucial to consider. Snugly fitting cuffs can prevent current leak but can also cause the nerve to crush and die after post-surgical expansion [36, 37].

Continued iteration and improvement of the cuff electrode developed with the introduction of multi-contact cuff electrodes [38] that utilized longitudinal grooves and four sets of tripolar arranged contacts. Polyimide-silicone hybrid cuffs were developed to stabilize and lower the bulkiness of multi-contact cuffs [39]. These cuffs have shown promise for being able to increase selectivity in stimulation and recording over previous iterations.

These examples of cuff electrodes focus on interacting with the natural geometry of the nerve without invasive disturbance, but cuff electrodes exist that seek to shape the nerve for recording and stimulating.

Slowly Penetrating Interfascicular Nerve Electrode

One downside of the cuff electrode is that it may be difficult to access the internal 'deep' fascicles within the nerve by using extraneural contact sites. The Slowly Penetrating Interfascicular Nerve Electrode (SPINE) used a spring structure embedded in a cuff to actively insert TIME-like structure over time [40]. This had limited success in being able to sufficiently insert functional contacts without damaging the nerve beyond repair.

Flat Interface Nerve Electrode

A later iteration of the SPINE focused on flattening the nerve to force it to remodel in a flattened state [41] to make all of the internal fascicles accessible to the extraneural contacts. This design has shown more success with further studies [42] in the femoral nerve to record and stimulate individual fibers with a verification in EMG recording. Further studies must be performed to analyze the chronic stability and biocompatibility of the structure.

1.3 The Common Failure Modus Operandi

The nature of failure in a chronically implanted electrode is a complicated and nuanced matter, but the primary concern of most researchers is the loss of functionality. To discuss the way in which electrodes chronically fail, it is important to discuss how an electrode and fiber couple for recording and stimulation. It is also important to recognize current trends in measures of chronic stability so that a synthesis of the topics has tangible meaning.

1.3.1 Electrode-Fiber Coupling

The basis of electrode-fiber coupling originates in the formulation of reciprocity, lead field theory, and the synthesis of the volume conductor as a spatial filter.
The reciprocity theorem, first introduced by Hermann von Helmholtz [43], is the theoretical basis for the lead field theory. By applying a unit reciprocal current, I_r, to a spatial volume source, J_i, the lead scalar potential field, Φ_{reci}, can be determined [44]. By following the the theory of reciprocity, the application of the negative gradient to Φ_{reci} results in the electric field E_{reci}. The electric field E_{reci} and the reciprocal current density field J_{reci} in an isotropic medium are related by the scalar multiplication of the conductivity, κ. This is summarized in Equation 1.1.

$$J_{reci} = \kappa E_{reci} = -\kappa \nabla \Phi_{reci} \tag{1.1}$$

In fact, the reciprocal current density field cannot by measured easily in an experimental environment. It is more practical to measure or examine voltage-potential signals. The relationship between the electric potential V_e and the volume current source J_i was derived by Plonsey [44] through Equation 1.2:

$$V_e = \int_v \frac{1}{\kappa} J_i \cdot J_{reci} dv \tag{1.2}$$

To understand how changes in fundamental, material conductivity of a volume conductor relates to changes in impedance, the concept of the transfer impedance, Z_t, was developed [45]. The estimation of Z_t can be done with a measured electric potential V_e and an applied current source I_r [44] through the application of Ohm's law: $Z_t \approx V_e/I_r$. However, the relationship between a current source electrode and voltage measuring electrode is defined in Equation 1.3.

$$Z_t = \int_v \frac{1}{\kappa} J_i' \cdot J_{reci} dv \tag{1.3}$$

In this relationship, J_i' is the uniform current density where $J_i' = J_i/I_{reci}$ to normalize the density to any amount of current supplied in I_{reci}. Further definition

of the contribution of unit volumes in the volume conductor from Equation 1.3 for sensitivity, S, is defined as $S = J_i' \cdot J_{reci}$. The sensitivity measure is fundamental to determine the influence of the field on the influenced medium. In the case of common monopolar or bipolar configurations the source and reciprocal current densities are identical [46], and thus, the transfer impedance of a unit voxel reduces to a function where $J = J_i' = J_{reci}$ and $S = |J|^2$. With this information it can be determined that examining the distribution of sensitivity through the transfer impedance can aid in the characterization of the electrical coupling of current source and voltage measuring systems in a conductive medium.

In context of applications in tissue engineering, the concept of transfer impedance has been used as a means to characterize and measure tissue impedance using various electrode configurations and techniques [47–49]. In the application of neural tissue, it is possible to consider the active nerve fiber as a current source and an electrode as a voltage measuring system. The coupling of the two can be analyzed in the context of transfer impedance but the changes in the extracellular space and its influence on coupling is explained through the volume conduction theory.

The fundamental work of Lorente de Nó [50] on the mathematical modeling of intracelluler and extracellular fields of a nerve fiber via action potentials in a volume conductor laid the ground work for various detailed analyses in multiple theoretical studies [51–53]. From this work, it is known that the electric potential field, Φ, in a homogeneous, isotropic material is governed by Maxwell's equations and can be reduced to the Poisson equation, shown in Equation 1.4.

$$\nabla^2 \Phi = -I_v/\kappa \tag{1.4}$$

From Equation 1.4, if the current source lies outside or at the boundary of the volume conductor, the equation can be reduced to Laplace's equation ($\nabla^2 \Phi = 0$). When solved using time-variant and quasi-static conditions, the cylindrical coordinate extracellular potential field in an infinitely conducting homogeneous medium can be characterized as a modified Bessel function of the second kind [54]. It is then deducible

that the extracellular space of a volume conductor acts as a spatial low-pass filter on the current source nerve fiber activity [55–57]. This means that the extracellular space's volume conduction filtering effects have a significant influence on the waveform of the action potential.

To describe the relationship between the field measuring point and the extracellular waveform, Plonsey proposed a convolution based approach [58]. Explicitly, this method relates that any point in the extracellular potential field is a convolution of a weighting function and the second derivative of the transmembrance potential. It is known by the work of Lorente de Nó [50] that the transmembrane current density is proportionally related to the second derivative of the transmembrane potential and therefore the extracellular potential, Φ_e, can be interpreted as the convolution described in Equation 1.5 where i_m is the transmembrane current density and w is the weighting function [53, 56] expressed in cylindrical coordinates:

$$\Phi_e(r, z, t) = i_m(r, z, t) * w(r, z) \tag{1.5}$$

The weighting function is described by the axial (z) and radial (r) distances of the field measurement point to the current source of the fiber. The amplitude of the measured extracellular action decreases as a function of increasing radius [58]; and thus, it is an important recognition that the ability to record a nerve fiber's activity is largely influenced by relative electrode-fiber distance and the conductivity of the medium. This is a key factor in the chronic performance of implanted electrodes, and through the lens of reciprocity can also greatly affect the ability of an implanted electrode to stimulate the nerve.

1.3.2 Recruitment Curves in Chronic Electrode Implantation

A common way to measure the stability of an implanted electrode is through the creation and analysis of recruitment curves. First discussed by Pierre Rabischong [59] in acute canine experiments in 1973, recruitment curves measure the ability of

an electrode to affect an end organ's response sensitivity to amplitude, frequency, and pulse width in stimulation. In the work by Rabischong, the force induced by contraction in the muscle of the canine was related to the electrical stimulation as well as the duration of the contraction. Conceptually, changing the stimulation intensity and frequency would cause functionally distinct activation of different fibers in the nerve or muscle to induce varying responses.

Later work by McNeal et al. [60] established that recruitment curves that are characterized after chronic implantation of an electrode have large variability in an adult feline sciatic nerve model. Additional work of implantable electrodes in the peripheral nerve and muscle [21, 61–63] has shown that change in recruitment curves over time is significant. Polasek et al. [61] noted that threshold for stimulation varied greatly with a cuff electrode in human implantation over the first fifteen weeks including total failure for stimulation recruitment. Jung et al. [62] showed that recruitment of muscle stimulation in rats varied with up to 300% baseline stimulation threshold after six weeks of implantation. Harreby et al. [21] showed that stimulation threshold increased over the implant time up to 500% greater than baseline stimulation threshold and in some cases the implants failed entirely.

It is apparent that the the environment of the electrode is changing post-implantation. These changes causing increased stimulation through drastically increased medium impedance are a significant hurdle in creating permanent, compatible implants.

1.3.3 The Influence of Encapsulation on Chronic Stability

With the known changes in chronic stability of implanted electrodes relating to the environmental change, it is inevitable to examine the commonly observed phenomenon of connective tissue encapsulation of electrodes.

Branner et al. [64] examined over 400 μm of encapsulating connective tissue around the tips of an intrafascicular electrode array. In this same study it was determined that

potential measured by the electrode dramatically dropped over time and stimulation threshold increased significantly up to failure in some cases.

This is a noticeable trend in even varying electrode types. It has been seen in TIME configurations that encapsulation connective tissue thickness in excess of 115 μm is seen in a sub-chronic implant [21,65]. It was also noted that LIFE configurations induced continued inflammation through macrophage recruitment well after 90 days of implantation causing instability [66]. Even less invasive designs such as a spiral cuff have shown a propensity for failure in mobile regions due to increased irritation [67].

To be more clear, even in the simplest design configurations, electrodes are being pushed away from their electrical activity source and are becoming less efficient or incapable of performing their function. The relationship between the electrode placement and long term stability is clear through a search in the literature. As electrode technology advances to enhance the design criteria of selectivity, reach, coherence, and correlation the minimized invasiveness and biocompatibility must also improve to take advantage of these improvements. Only by using modern techniques for design and investigating sources of continued can the chronic electric stability issue be solved.

1.4 Problem Statement

Work by Qiao [68] and Horn [69] explores the relationship between spatial characteristics of a medium and the ability of an electrode to couple with a fiber. The medium acts as a spatial filter to determine the characteristics of a signal that can be detected by the recording configuration. Experimental observation of recruitment curves in chronically implanted electrodes shows that the stimulation characteristics are significantly affected by the encapsulation of an electrode and that it may be a cause for total failure. Through an understanding and application of reciprocity, it is possible that the ability of an electrode to both stimulate and record from a fiber is

affected by the connective tissue encapsulation, which can be described by weighting function.

However, the examination of how the implantation affects the encapsulation is not solely an electrical problem. The experience of many physicians and researchers shows that the large mechanical and geometrical mismatch of implantable systems is a source of functional failure, particularly through fibrotic encapsulation [70, 71]. The focus of this work is to explore the mechanical properties and relationship of implantable electrodes with the peripheral nervous system.

1.4.1 Hypothesis

One of the primary sources of failure in implanted electrodes is due to encapsulation of the electrode. It is important to note that the encapsulation of an electrode is not necessarily a sign of impending electrode failure. As noted by Grill and Mortimer [72], encapsulation tissue can serve as a natural anchor for a cuff electrode that prevents it from moving during locomotion. It is not known in what way the mechanical properties of an electrode contribute to the specific immune response as to whether or not there will be too much fibrotic encapsulation to cause chronic failure. We hypothesize that this encapsulation is due to a strain mechanism and that it is necessary to fundamentally characterize the relationship between the strain environment of the nerve and the material properties of the electrode.

By using advanced modeling techniques in conjunction with mechanical testing and histology, we will be able to determine the fundamental mechanical interaction of an electrode and a nerve. We hypothesize that the strain environment of the implant zone induces a continuous shear effect. By understanding this mechanism a cuff or stent device could be designed in the future to reduce the stress of the implant site and control encapsulation to be used as an advantageous design criterion.

1.4.2 The Use of Finite Element Analysis in Tissue Applications

A search of any literature source for the use of finite element analysis (FEA) shows that it is a valuable tool widely in use. This widespread use is because FEA has several advantages that conventional pen and paper analysis is incapable of comparing to: complex geometry can be easily represented, wide variation in material property can be easily included, the representation of different solution is easily performed, and the local effects of complex conditions can be captured [73].

This fundamental advantage comes from the flexibility and application of creating a finite element model (FEM) for analysis. Geometric domains are created and given distinct material properties that are necessary for computation for mechanical, electrical, thermal, and fluid dynamic analysis. These geometric domains interact through boundary relationships. Loading conditions can be defined, a mesh of differential equation matrices is created and when set sufficiently a solution can be generated and analyzed. This creation and analysis of the FEM is dependent on accurate representations of geometry and accurate estimates of the innate properties of the material. Obtaining this information is often aided through the use of imaging techniques and validation testing to measure geometry and isolate material properties.

In biomedical applications, FEA has aided in complex computations of many scenarios and conditions such as knee joint loading [74], heel pad load distribution in gait [75], tibial ligaments loading [76], mastication loading [77], arterial elastic loading [78], cardiac valvular mechanics [79], and many more. By accurately representing the material properties and geometry of tissues it is apparent that valuable information and solutions can be obtained from the use of FEA.

1.4.3 The Use Of Tensile Testing in Soft Tissue

The use of tensile or elongation testing in soft tissue is not a new technique; it is well characterized and understood. Yuan-Cheng Fung, the father of modern biomechanics, discussed the limitations and methodology of tensile testing to great

extent [80]. For measuring elasticity in this method, the most significant factor to consider as interference is the viscosity of the material [81]. As Fung explained, the viscous property of living tissue contributes to inherent hysteresis and non-linearity. Through testing he determined that simple repeated cycling of loading conditions reduced the amount of hysteresis and aided in linearizing the elastic curves for measurement.

In performing these tests, the viscosity of the material is not the only important factor at play. The hydration of the tissue significantly impacts the performance of the tissue in mechanical testing, and another important consideration is the process of excision. In arterial tissue, Fung showed that the existence of residual stresses in the artery significantly changed the behavior of the tissue in elongation testing and modeling of stretch [82] and later noted that the effects of residual strain were evident in other tissues such as cardiac muscle [83], the trachea [84], and the gastrointestinal tract [85].

In later discussions, Fung postulated that there is a theoretical law in effect that relates strain to arterial and other soft tissue growth [6] in a similar manner in which bone density changes as a function of strain [86] through the application of Wolff's law [87]. It is this theoretical law that may drive the effects of electrode rejection in the nervous system.

1.4.4 The Use Of Imaging Techniques In Soft Tissue Deformation

By examining soft tissue in mechanical testing, it is known that whole material properties are being measured. In many simplified geometries assumptions can be made about the uniformity of the load distribution, but techniques such as digital image correlation have been developed to measure strain as a function of location in soft tissue. Zhou et al. [88] developed a speckle patterning technique to track the changes of small deformations in two dimensions of dissected aorta. Thompson et al. [89] developed a technique to measure localized strain in the region of a callus to

predict loading outcomes using natural surface markers. A technique for measuring localized strain in uniaxial loading of soft tissue was developed as well by Doehring et al. [90] using the light deflecting properties of collagen.

By adding an implantable electrode to a nerve, the geometry of the testing environment becomes more complex, and it becomes necessary to examine the effects of the electrode on the localized tissue strain environment. The use of sophisticated imaging techniques will allow for a better understanding of the localized effects and influence of the material properties of the electrode.

1.4.5 Flexible Shape Memory Polymers

It is well known that the geometric and mechanical mismatch of implants and tissue is a source for constant failure [70, 71]. This mismatch results in biological restriction and aggravation of the foreign body response, which is especially exacerbated in soft tissues such as the nervous system. The development of softer and more flexible electrodes is a critical turning point in implantable systems to better enable biocompatibility during implantation.

A leading development in this field is the creation of a shape memory polymer (SMP) [91, 92] based cuff electrode to interface with the nervous system. This application of thiol-ene polymer electrode is stiff at room temperature and softens to a tunable range of 6-600 MPa modulus at body temperature. The use of such a material enables an electrode that is stiff enough to implant with ease, but soft enough after implantation to have a lower likelihood of continuous agitation.

1.4.6 Specific Aims

Using the techniques of finite element analysis, mechanical tensile testing, and imaging in nervous tissue deformation the present work addresses the characterization of the mechanical relationships between the nerve and the material properties of the electrode through the following specific aims:

1. Create and develop a histologically informed finite element model (FEM) to analyze the strain environment of a nerve and shape memory polymer (SMP) cuff electrode.

2. Demonstrate a reduction of strain in the nerve using ex-vivo tensile mechanical testing with shape memory polymer (SMP) cuff electrode attachment.

3. Demonstrate the location and geometry dependence of strain reduction in the nerve during ex-vivo tensile mechanical testing using digital image correlation techniques and finite element analysis (FEA).

In Chapter 2, specific aim 1 is addressed by excising the vagus nerve of a canine model. It is obtained and standard hematoxylin & eosin (H&E) staining is performed to analyze the geometry of the cross sectional area of the nerve. A simplified model of a shape memory polymer (SMP) cuff electrode is attached to a geometric representation in the FEM where a residual tensile load is applied to compare strain environments after attachment.

In Chapter 3, specific aim 2 is addressed by excising the vagus nerve of a canine model. Tensile mechanical testing is performed to compare the strain relationship of the nerve to an electrode-attached counterpart.

In Chapter 4, specific aim 3 is addressed by excising the vagus nerve of a canine model. An array of visual markers are transferred to the nerve and tensile mechanical testing is done with digital imaging tracking the strain in the nerve and its electrode-attached counterpart. This observation is validated with a finite element model and solutions for solving potential issues are proposed.

By addressing these aims the mechanical relationship of the initial functional attachment of a less-invasive cuff electrode to the nerve can be determined to move towards intensive in-vivo studies of chronic implantation.

2. FINITE ELEMENT MODELING TO ANALYZE STRAIN

The widespread use of finite element analysis (FEA) is because it has several advantages that conventional pen and paper analysis is incapable of comparing to: complex geometry can be easily represented, wide variation in material property can be easily included, the representation of different solutions are easily performed, and the local effects of complex conditions can be captured [73].

This fundamental advantage comes from the flexibility inherent in creating a finite element model (FEM) for analysis. Geometric domains are created and given distinct material properties that are necessary for computation for mechanical, electrical, thermal, and fluid dynamic analysis. These geometric domains interact through boundary relationships. Loading conditions are defined, a mesh of differential equation matrices is created and a solution can be analyzed.

2.1 Development of The Finite Element Model

The creation of the FEM is dependent on the geometric fidelity of the model. In this chapter, a FEM was developed to compare the strain environment in different models of the nerve. A laminar model was developed with distinct domains dedicated to the endoneurium, perineurium, and epineurium and was then compared to a bulk model where there was a singular nerve domain. The geometry of the nerve and its sub-domains are informed by the use of a histological procedure and image processing. Finally, an extraneural cuff was modeled and fit to the surface of the nerve to evaluate the strain environment upon axial loading of the nerve.

The values of the intrinsic material property of the nerve, and soft tissue, are debated and range in value from hundreds of pascals (Pa) to Megapascals (MPa) [93].

It was important to maintain the characterized relationship in a laminar model of a stiff, thin sheet that bears much of the load as the perineurium [94], an epineurium up to 100 times less stiff than the perineurium [94], and an endoneurium that was in between the stiffnesses depending on the axonal density of the nerve [95, 96].

For the laminar model, the endoneurium region was given a modulus value of 100 kPa and a Poisson ratio of 0.4. The perineurium was given a sheet stiffness of 10^6 N/mm and the epineurium was given a modulus of 10 kPa and a Poisson ratio of 0.4. The values given are based off of literature values and ranges discussed previously by Sunderland and Borschel [93, 95]. For the bulk model, the nerve was given a modulus of 500 kPa and a Poisson ratio of 0.4. In the bulk nerve model, the cuff was based off a shape memory polymer (SMP) electrode and was given a modulus of 5 MPa with a Poisson ratio of 0.3. Its dimensions were 7 mm in length, 100 μm thick, and fits the circumference of the nerve perfectly.

The boundary conditions and loads of the model were consistent in each iteration. The nerve was pulled in tension at each end with a 70 mN/1.75 mm^2 load. The cuff was attached to the nerve with two no-slip boundary conditions where the inner diameter edge of the cuff was perfectly and rigidly attached to the nerve. This was seen as an ideal attachment case where the cuff is touching the nerve but there is no slipping at either end of the cuff and could ideally by achieved *in vivo* using sutures, surgical glue, or any other number of applications. The geometry of the nerves was informed by doing histochemical staining of canine vagus nerves and measured using ImageJ software to discriminate and measure the various domains of the nerve. All modeling and analysis of the FEM was performed using COMSOL Multiphysics® version 5.1. Table 2.1 summarizes the assigned material properties for the various components of the nerve in both the laminar and bulk nerve models.

Table 2.1.: Summary of the material properties assigned to the various components of the nerve in FEM from literature values. †The Perineurium does not have a Young's Modulus in the laminar model, but rather has a sheet stiffness of $10^6 N/mm$ and therefore also does not have a Poisson ratio assigned to it.

	Young's Modulus	Poisson's Ratio (ν)
Endoneurium	100 kPa	0.4
Epineurium	10 kPa	0.4
Perineurium†	-	-
Bulk Nerve	500 kPa	0.4

2.1.1 Geometric Properties From Histology Analysis

With considerations being made to the material properties of the nerve, the first step in developing the model was to gather data that informs the dimensions of the model. A simple and cost effective method for gathering this information is to perform histology and use image processing programs to gather dimensions. For the development of this model, the canine vagus nerve was excised and subjected to hematoxylin & eosin (H&E) staining and the dimensions of the domains were measured in ImageJ.

Hematoxylin & Eosin Histological Procedure

To perform H&E staining, the canine vagus nerve was excised following euthanasia of the canine by the Indiana University (IU) Laboratory Animal Research Center (LARC). The nerve was then preserved in 10% neutral phosphate buffered formalin before being embedded in a paraffin block. The block was then sectioned at 10 μm and the sections were stained. This was done by first washing the section in a hematoxylin solution for one to ten minutes, depending on the strength of the solution. Next, the section was washed in distilled water carefully before washing in eosin solution for

approximately one dozen agitating submersions. Next the section was washed in six consecutive single submersion containers of 195 proof (97.5%) ethanol before being clarified with six submersions in xylene. After air drying, the section was mounted with acrytol and taken to imaging. The sections were then imaged using a Nikon ® Eclipse series microscope.

Figure 2.1 is an example of the results of the histological procedures where there is a clearly defined perineurium membrane enveloping the endoneurium and it is wrapped in the folding, loosely connected epineurium. Other stains are available that could accomplish a similar imaging goal, such as Masson's trichrome, but the simplicity and effectiveness of the H&E procedure makes it a valuable tool for this assessment.

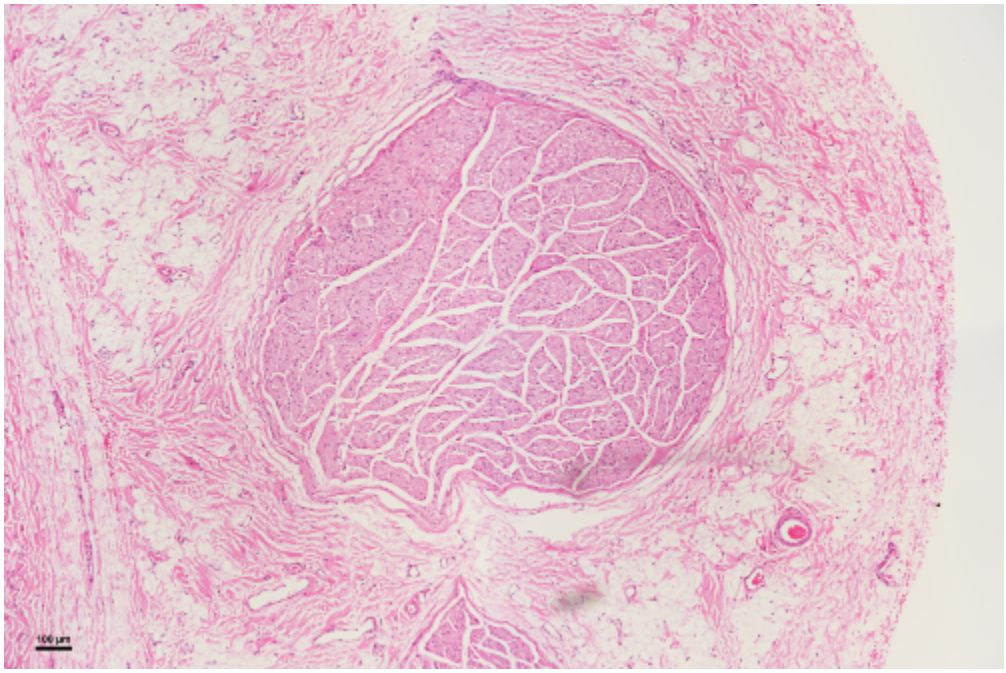

Fig. 2.1.: An example histological cross section of a canine vagus nerve after hematoxylin & eosin staining to visualize the endoneurium, perineurium, and epineurium domains.

Geometric Measurements of The Canine Vagus Nerve

After the nerve was stained and imaged, the images were imported into ImageJ. The perineurium interior edge was traced and the circumference of the resulting ovular approximation was recorded. Between 80 and 100 radial measurements were then taken from the interior perineurium membrane edge to the exterior edge to determine an average thickness of the perineurium. The exterior membrane edge of the epinerium was traced and the circumference of the resulting ovular approximation was recorded. Another 40 to 60 radial measurements are taken from the exterior membrane edge to the exterior edge of the perineurium to determine the average epineurium thickness.

The results of these measurements show that the average perineurium thickness of the canine vagus nerve was 13.63 $\pm$ 5.54 μm with an average circumference of 4.146 mm. The epineurium of the canine vagus nerve has an average thickness of 172.67 $\pm$ 64.20 μm with an average circumference of 5.156 mm. It is important to consider that the diameter of the nerve used in the FEM was made by taking the circumference of an ovular approximation and finding the diameter by using a circle approximation meaning the nerve diameter is 1.5 mm in the models.

2.2 Results of the Finite Element Models

The results of the FEM indicate that there is a similar behavior between complex laminar models and a simplified bulk model. Figure 2.2 indicates that the axial strain in a bulk and laminar model is similar in nature of bearing the load, but the strain is a different value.

This strain value can be examined more precisely by creating an extraction line through the central axis of the nerve. This allows the examination of the value from end-to-end to examine if there are geometric effects. This same method is used consistently to examine the effects of the addition of flexible SMP cuffs as well.

Table 2.2.: A summary of the histological measurements made of the canine vagus nerve.

				Perineurium			Epineurium		
Age	Sex	Weight (lbs)	Left or Right	Thickness (avg. μm)	Thickness (std. μm)	Circumference (mm)	Thickness (avg. μm)	Thickness (std. μm)	Circumference (mm)
1 yr	M	63	R	15.73	6.44	3.992	255.48	74.10	5.177
1 yr	M	59	R	13.68	5.81	3.943	222.10	69.79	5.489
1 yr	M	59	L	11.27	4.93	3.677	146.04	30.89	4.609
1 yr	F	44	R	12.61	6.28	3.440			
1 yr	F	44	L	9.68	3.99	3.698	196.79	120.10	4.799
1 yr	M	42.8	R	9.08	3.29	4.033	123.30	43.60	4.637
1 yr	M	42.8	L	13.81	7.17	4.022	138.79	40.45	4.935
1.5 yr	M	61.8	R	11.51	4.41	3.921	95.08	46.88	4.399
1.5 yr	M	61.8	L	19.14	9.54	4.393	216.2	105.9	5.934
1 yr	M	55.6	R	21.03	6.31	5.026	180.91	46.16	6.116
1 yr	M	55.6	L	14.49	6.38	4.521	171.24	76.52	5.521
1 yr	M	58.6	R	13.04	3.99	4.961	258.22	114.53	5.84
1 yr	M	58.6	L	12.93	4.19	4.689			
9 mo	M	68	R	12.26	4.31	3.867	143.65	46.36	4.774
9 mo	M	68	L	14.16	6.01	4.002	96.95	19.28	4.801
			Average	13.63	5.54	4.146	172.67	64.20	5.156

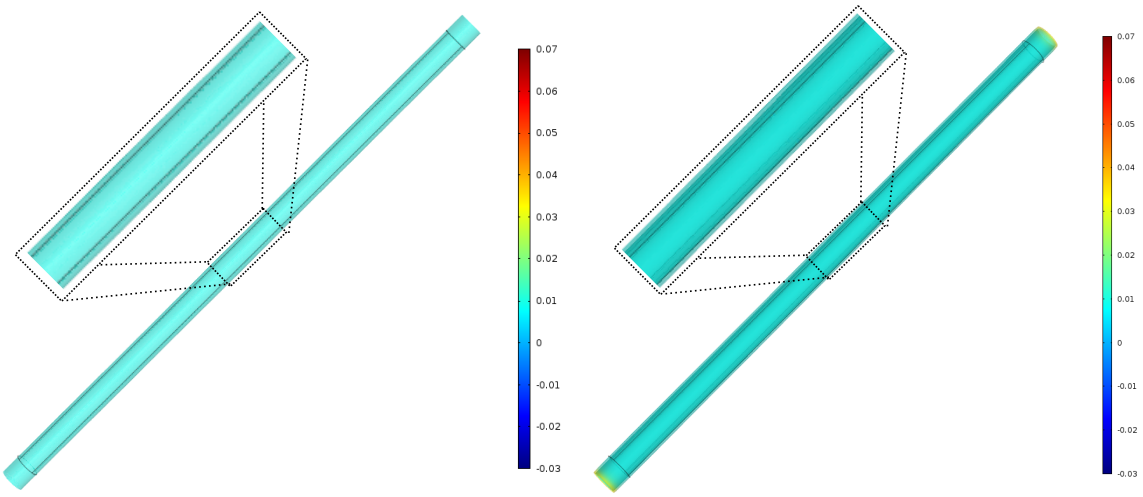

(a) Bulk Nerve FEM (b) Laminar Nerve FEM

Fig. 2.2.: The finite element model axial strain results of stretching the bulk nerve model in tension with loads of 70 mN at each end, a modulus of 1 MPa, and a Poisson ratio of 0.4 is indicated in 2.2(a). The finite element model axial strain results of stretching the laminar nerve model in tension with loads of 70 mN at each end. The endoneurium is given a modulus of 100 kPa and a Poisson ratio of 0.4, the perineurium is given a sheet stiffness of 10^6 N/mm, and the epineurium is given a modulus of 10 kPa and a Poisson ratio of 0.4 is indicated in 2.2(b).

Figure 2.3 shows that the difference between the bulk and laminar nerve models is a difference of 18.414 $m\varepsilon$ in the bulk nerve model and 17.460 $m\varepsilon$ in the laminar model. Both nerve models conduct consistent axial strain as a function of the length of the nerve. A major difference in the models is computational complexity. The addition of a thin sheet domain and two separate domains for the endoneurium and epineurium increase the mesh size. In achieving similar results with a small difference of strain, the continued analysis of the nerve with the addition of a cuff uses the bulk nerve as its central model.

Figure 2.4 shows that in the same loading environment there is a strain reduction in the region of the cuff with an increase in strain at the cuff boundary regions.

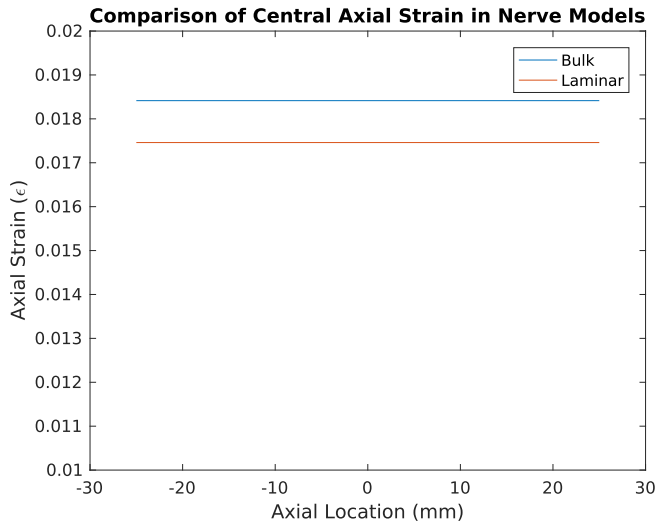

Fig. 2.3.: A comparison of central axial strain in the bulk and laminar nerve models by extracting the axial strain component along a central line through the geometry of the nerve model. The abscissa reads from left to right as from one end of the nerve to the other along the central axis.

By examining the axial strain as a function of nerve length the information about the strain reduction mechanism.

Figure 2.5 shows the comparison of strain along the length of the models. Outside of the cuff region, the models bear an equal strain of 9.207 $m\epsilon$. In the region of 1.5 mm outside of the cuff on either end, the nerve and cuff model has an increased strain of 9.301 $m\varepsilon$. Once reaching the center point of the nerve, the strain is reduced to 0.827 $m\varepsilon$. From the edge of cuff at $\pm$3.5 mm there is another artifact of strain magnitude change. This is a result of the principle angles of the nerve changing as the boundary conditions of the nerve change from nerve region to nerve and cuff region, causing anti-clastic strain forces to form as the axial strain reduces by a factor of nearly ten.

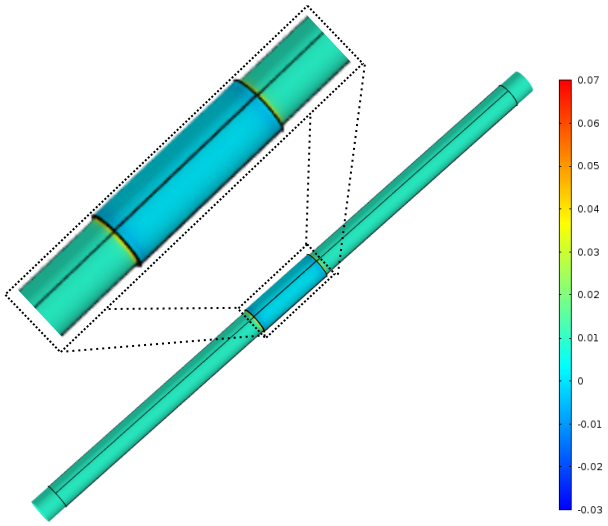

Fig. 2.4.: The finite element model axial strain results of stretching the bulk nerve model in tension with loads of 70 mN/1.5 mm^2 at each end, a modulus of 500 kPa, and a Poisson ratio of 0.4. The cuff attached is a shape memory polymer cuff with a modulus of 5 MPa and a Poisson ratio of 0.3

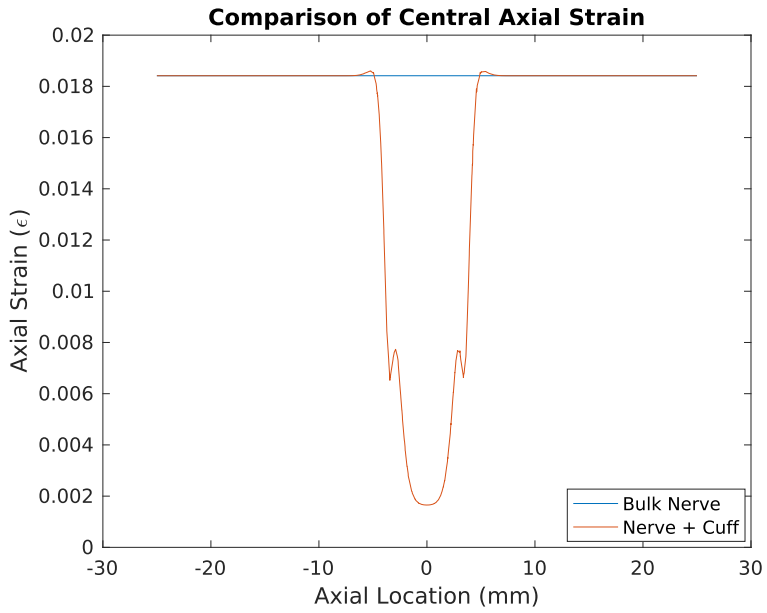

Fig. 2.5.: Comparison of the central tensile axial loading of the nerve and the nerve with a cuff attached using the no-slip boundary condition. The abscissa reads from left to right as one end of the nerve to the other end along the central axis.

2.3 Conclusions of the Finite Element Models

The differences of the laminar and bulk nerve models is a difference of approximately 5% in terms of strain value with no change in the characteristic mechanism of equal loading along the length of the nerve. In terms of performance, the bulk nerve model model uses a mesh of size 10^6 elements and takes less than 3 minutes to fully compute a solution while the laminar model takes 10^8 or more elements and takes up to 7 minutes to compute a solution. In addition, the inherent variance of intrinsic material properties would lead us to resolve that increased of complexity for a 5% becomes unnecessary to the fidelity of the model.

The addition of a flexible shape memory polymer cuff to the nerve has implications to the long term chronic stability of the implant. If such a boundary condition can be achieved, the modulation in strain will dictate the encapsulation of the nerve. Highly stiff electrodes will induce larger strains in the tissue through increased weight and attachment to surrounding tissues while the flexible shape memory polymer decreases the strain. The use of a finite element model to predict the strain environment will aid in designing, manufacturing, and validation of future iterations of electrodes to examine the mechanical viability of the implant.

However, the question exists on the robustness of the FEM to capture the effects of the no-slip boundary condition. In the current simulation, eight quadrant circular arcs make the two no-slip boundary conditions of the cuff attached to the nerve. In addressing the robustness of the simulation, steps were taken to create a range of simulations that captured variation in the efficiency of the no-slip condition. In total, 28 simulations were run using the bulk nerve and cuff model, covering through symmetry all 256 combinations of the no-slip condition. Figure 2.6 shows that the variation of no-slip condition causes a change in the region of the cuff, but the overall strain environment is preserved. The least efficient condition of 2 quadrants of the cuff being the no-slip condition opposite each other has a strain in the center close to 0.01ε and when the cuff is fully effective, the strain is just under $.002\varepsilon$.

This information gives boundaries for design variation based on effectiveness of the no-slip and also indicates that the ability for the cuff to create a reduction in strain is dependent on the ability for the no-slip condition to be induced. If the implantation of the cuff is unable to achieve a perfect no slip condition with a cuff, there will still be some strain reduction somewhere between 10 and 100 times in the region of the cuff.

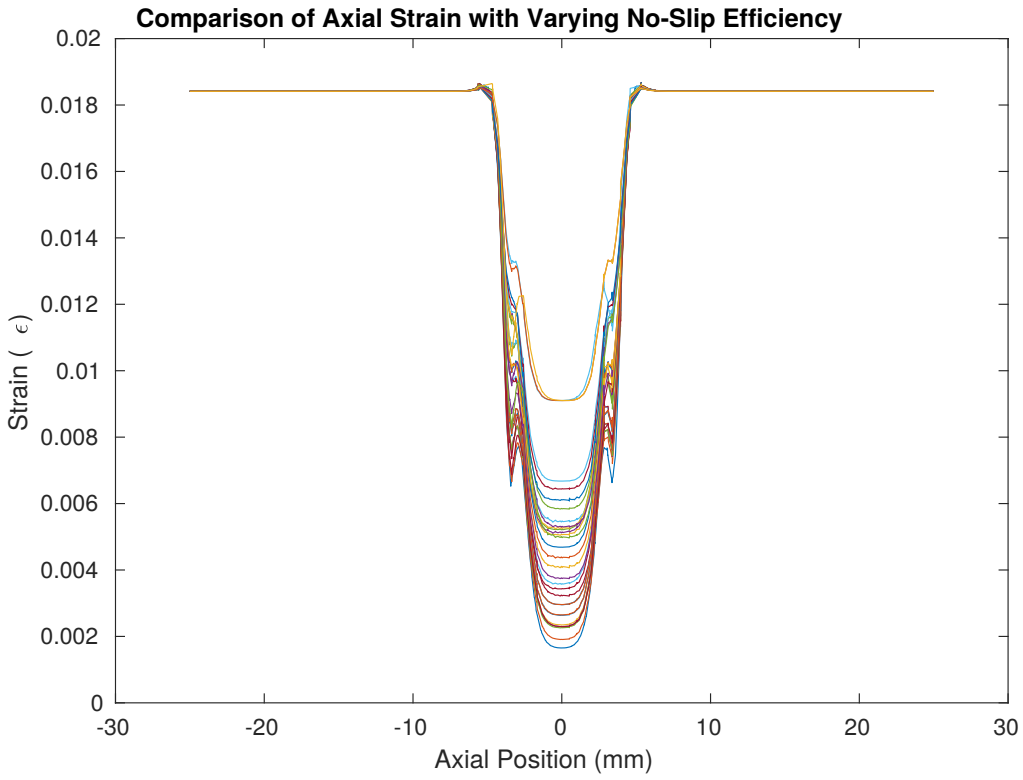

Fig. 2.6.: Comparison of the axial strains in the simulation by varying the effectiveness of the no-slip boundary condition

2.3.1 Extended Examination of the Laminar Model

Although there are seemingly small differences between the laminar and the bulk nerve models, the development of the unpredictably large boundary effects in the bulk model beget the need for a further examination of the effects in the laminar model. The cuff model as described in Section 2.1 is attached the laminar nerve in the same manner as the bulk nerve with the same loading conditions for comparison.

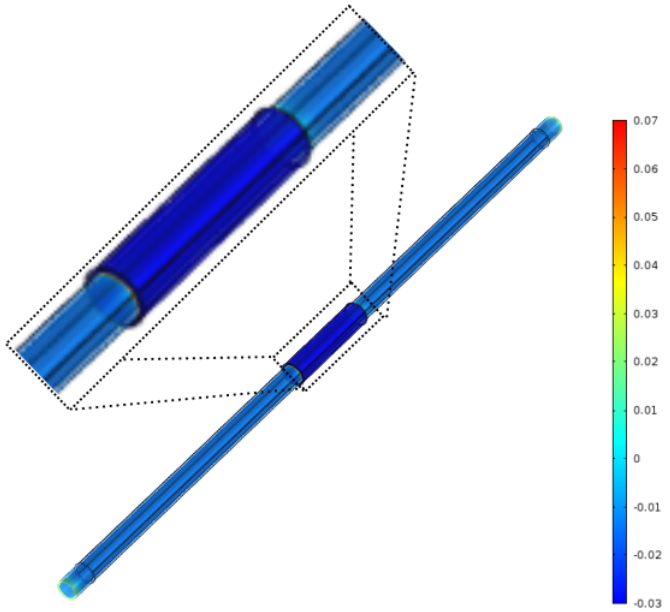

Fig. 2.7.: The finite element model axial strain results of stretching the laminar nerve model in tension with loads of 70 mN/1.5 mm^2 at each end. The cuff attached is a shape memory polymer cuff with a modulus of 5 MPa and a Poisson ratio of 0.3

Figure 2.7 shows the resulting FEM of the laminar nerve and cuff attachment. There is a similar stress concentration at the attachment of the cuffs, but the strain mechanism becomes more apparent when coming the strain as a function of length between the laminar and bulk nerve models. In Figure 2.8 it is apparent that there is a minor difference in steady-state strain, but the boundary effects due to the cuff attachment are much less pronounced in the laminar model. The ends of the nerve

experience a much more exaggerated boundary effect in the laminar model, but overall the strain reduces to a similar value.

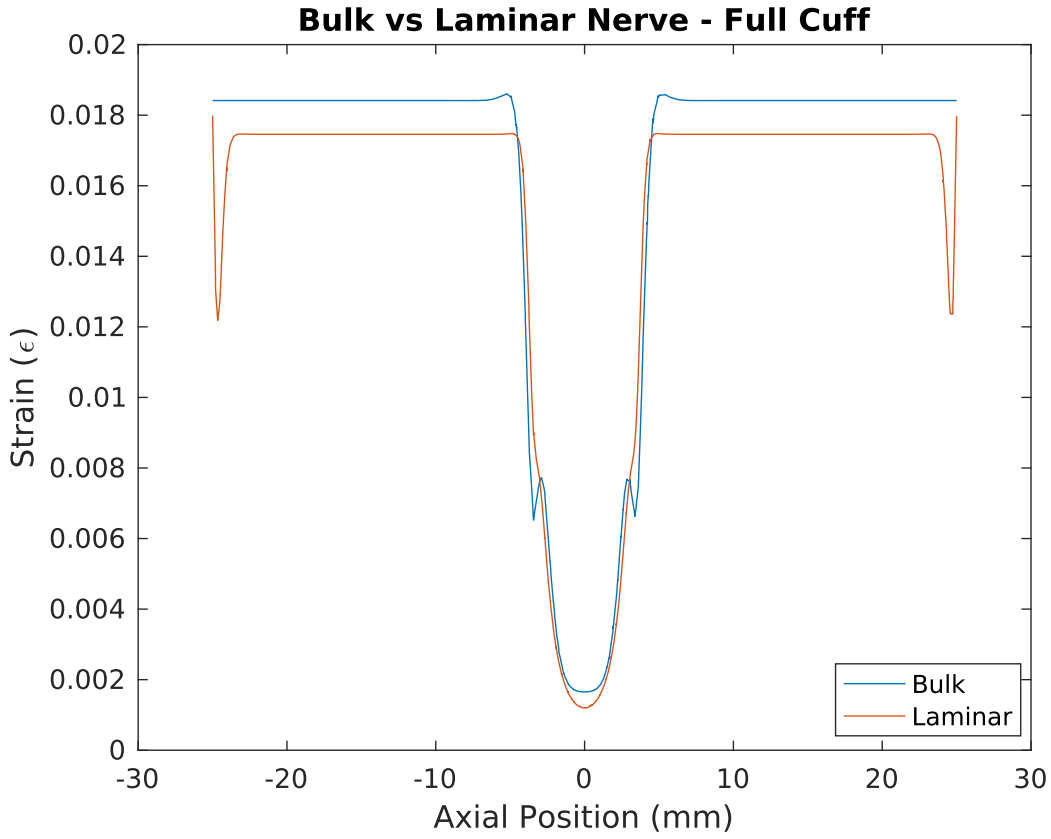

Fig. 2.8.: Comparison of the axial strains in the simulation with differences between the laminar and bulk nerve model. The laminar model includes boundary effects at the ends where surface loads are applied. The length of the nerve prevents boundary effects from interacting with the cuff region according to Saint-Venant's principle.

The differences between the models are subtle but could be important tuning parameters. The boundary effects have significance in the model and the laminar model's reduction of these effects could be due to factors such as perineurium membrane not transmitting the boundary effects from epineurium to endoneurium due to being a thin sheet. Further examination of these differences can be examined with future models that focus on these subtle differences.

3. EX-VIVO EXAMINATION OF STRAIN ENVIRONMENT USING TENSILE TESTING

The use of tensile or elongation testing in soft tissue is not a new technique; it is well characterized and understood. Fung discussed the limitations and methodology of tensile testing to great extent [80]. For measuring elasticity in this method, the most significant factor to consider as interference is the viscosity of the material [81]. As he explained, the viscous property of living tissue contributes to inherent hysteresis and non-linearity. Through testing he determined that simple repeated cycling of loading conditions reduced the amount of hysteresis and aided in linearizing the elastic curves for measurement.

Once the viscous components of a soft tissue are reduced and loading is performed, analysis of the force and displacement curves can be done to evaluate properties such as ultimate force and work to failure [97]. While this can be useful, for materials with variance in size and shape it is necessary to use the stress-strain curve by normalizing force applied to the area of a cross section. From this, the elastic modulus E can be found using the following relationship in Equation 3.1:

$$\sigma = E\varepsilon \tag{3.1}$$

Equation 3.1 is a variation of Hooke's Law [97] for springs that relates the strain, ε, to the stress, σ, through the slope of the curve as the elastic modulus, E. Simple tensile or compressive mechanical testing of a material can determine this value by measuring the slope of the stress-strain curve.

To understand the effects of an attachment or change to a material system, the modulus can be used to signify a change in the inherent material properties of the system by comparison. In this chapter, tensile testing is performed on a standardized

elastic material to measure differences between the material and the material when the SMP cuff is attached. Next, the same test is performed in excised canine vagus nerve to compare the modulus of the materials when a cuff is attached to determine if the cuff electrode changes the inherent mechanical properties of the system.

3.1 Methods for Mechanical Tensile Testing

The canine vagus nerve sections were excised after euthanasia according to the standards of the Indiana University (IU) Laboratory Animal Research Center (LARC) and stored in a phosphate-buffered saline solution for no more than two hours before tensile testing occurred. Testing occurred at a room temperature of 22°C.

To test the materials, the ends were fixed using alligator clips that have been soldered to Luer Lock needles that fit onto prefabricated test fixtures. For each material, the diameter of the approximately cylindrical objects were measured using a caliper and recorded to make area computations for use in analysis. The length between the fixed points was measured as the initial length of the material to convert displacement to strain during analysis. Attaching the shape memory polymer cuff to the materials required heating the cuff in a warm bath of 50°C for 5 minutes before applying it the material. The edge of the cuff received a light application of super glue (Loctite® 414™ Super Bonder®) using a hypodermic needle to apply the no-slip condition of the cuff.

According to the works of Fung [81], the first three cycles of loading will have the largest changes in viscoelastic response, but after this there should be minimal change indefinitely for cycles. Following this understanding, the nerves w1ere cyclically loaded 5 times to the same stretched length before the measured loading was analyzed. The materials were stretched at a rate of 0.5 mm/s to a designated length. Data were extracted and analyzed in MATLAB® R2016b to measure the slope of the stress-strain curve for the elastic modulus.

The tensile and mechanical testing system is a custom-built system, created by Drs. Ken Yoshida and Winnie Jensen [98]. The Vitrodyne V1000 system performs the tensile or compression actions, which is controlled by the JVL DMC10 controller. The Sensotec Model 31 load cell interprets the force and the SG010 strain gauge amplifier sends that signal to the National Instruments (NI) ® BNC 2111 data acquisition board. The Vitrodyne V1000 and the NI BNC 2111 data acquisition system communicate and synchronize with a Dell® Optiplex computer. Figure 3.1 shows a simple schematic with data flow indicated by the arrows. Data were analyzed in MATLAB® R2016b using a custom code to measure the slope of the stress strain curve. The groups are compared using a one-tailed Student's t-test to differentiate between groups with significance at a $p < 0.05$.

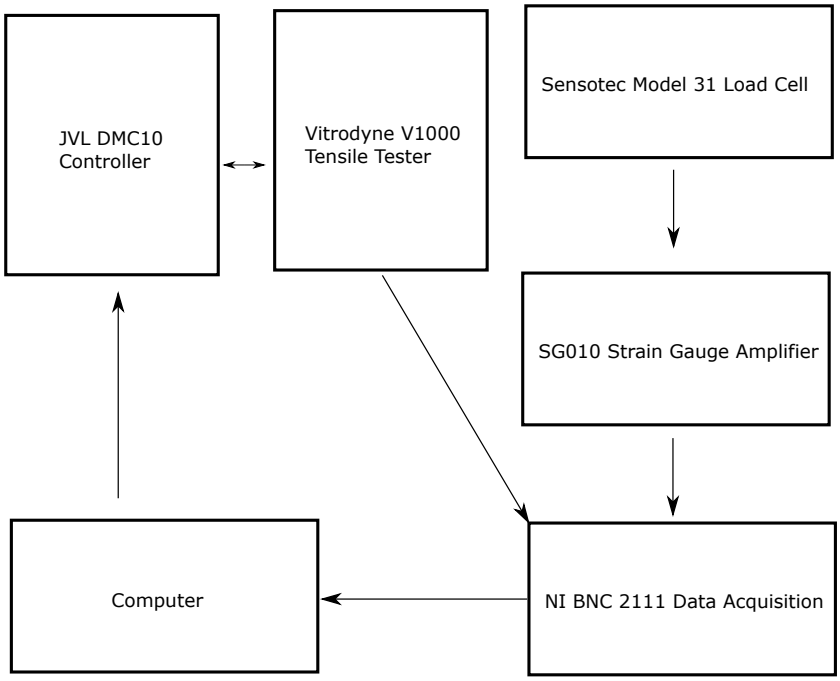

Fig. 3.1.: A schematic diagram of the tensile testing system to acquire data in mechanical testing with data flow directed by the arrows.

Custom LabVIEW® 2015 software synchronizes the tensile tester and load cell data while low-pass filtering the data to remove noise. It then extracted the data to a Microsoft Excel® .CSV file that can be analyzed using custom MATLAB® R2016b code. Figure 3.2 displays the front panel and settings able to be changed in the code.

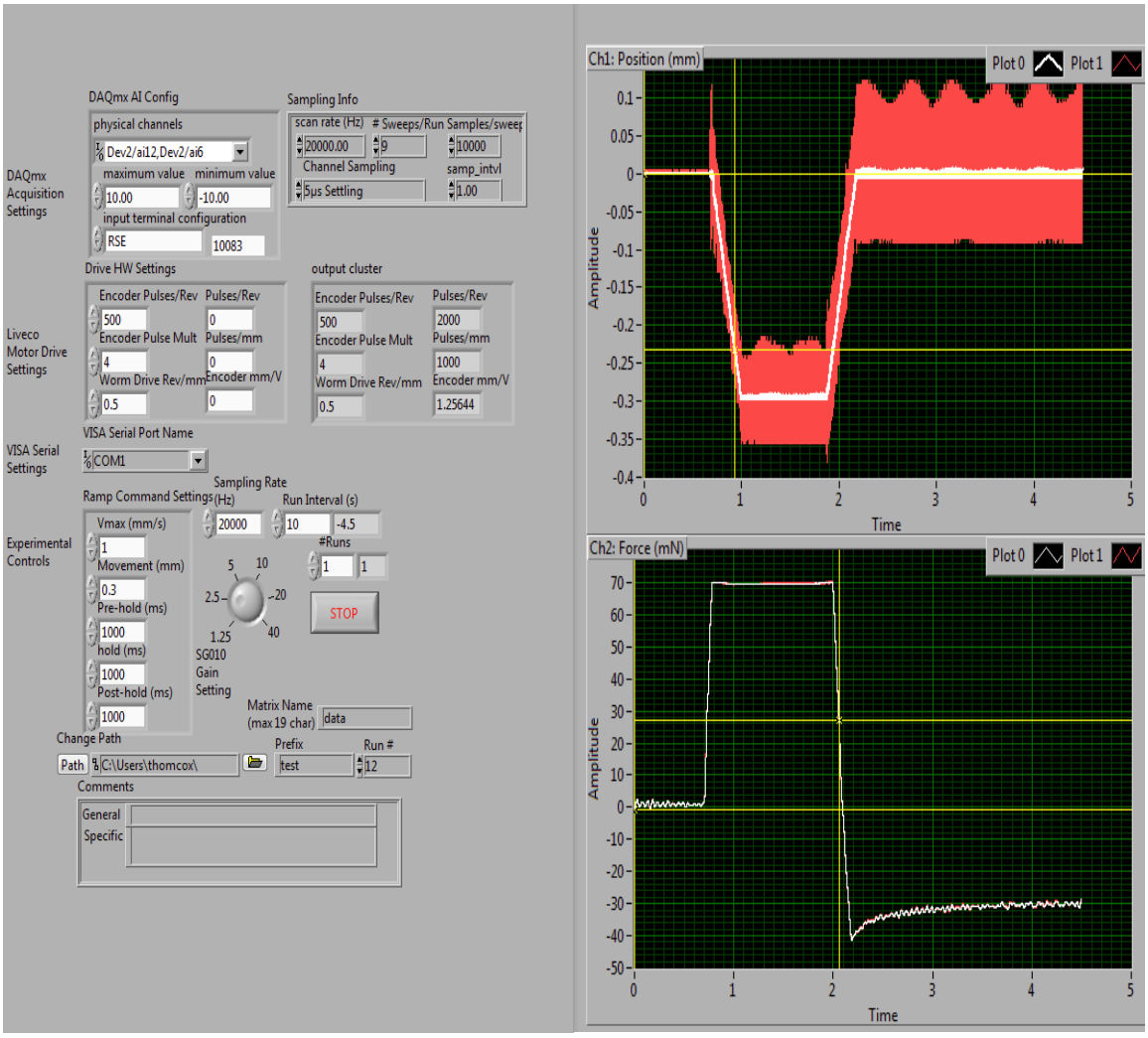

Fig. 3.2.: The custom LabVIEW® 2015 software built to integrate the tensile testing system and data acquisition system to control and measure through one system. The left panel allows the user to modify higher and lower level variables to control the tensile tester while the right panel displays the acquired data after being passed through a simple filter.

3.2 Results of Tensile Testing of a Standardized Material

The tensile testing procedures were done using the methods described in Section 3.1 for the standard elastic material. Figure 3.3 shows an example stress and strain curve comparison for the elastic test material with and without a cuff attached to it. The average elastic modulus measured during six tests for the control is 10.57 ± .07 MPa and the average elastic modulus for the test material plus the attached cuff is 11.93 ± .14 MPa. Using Student's t-test the groups are significantly different at $p < 0.05$.

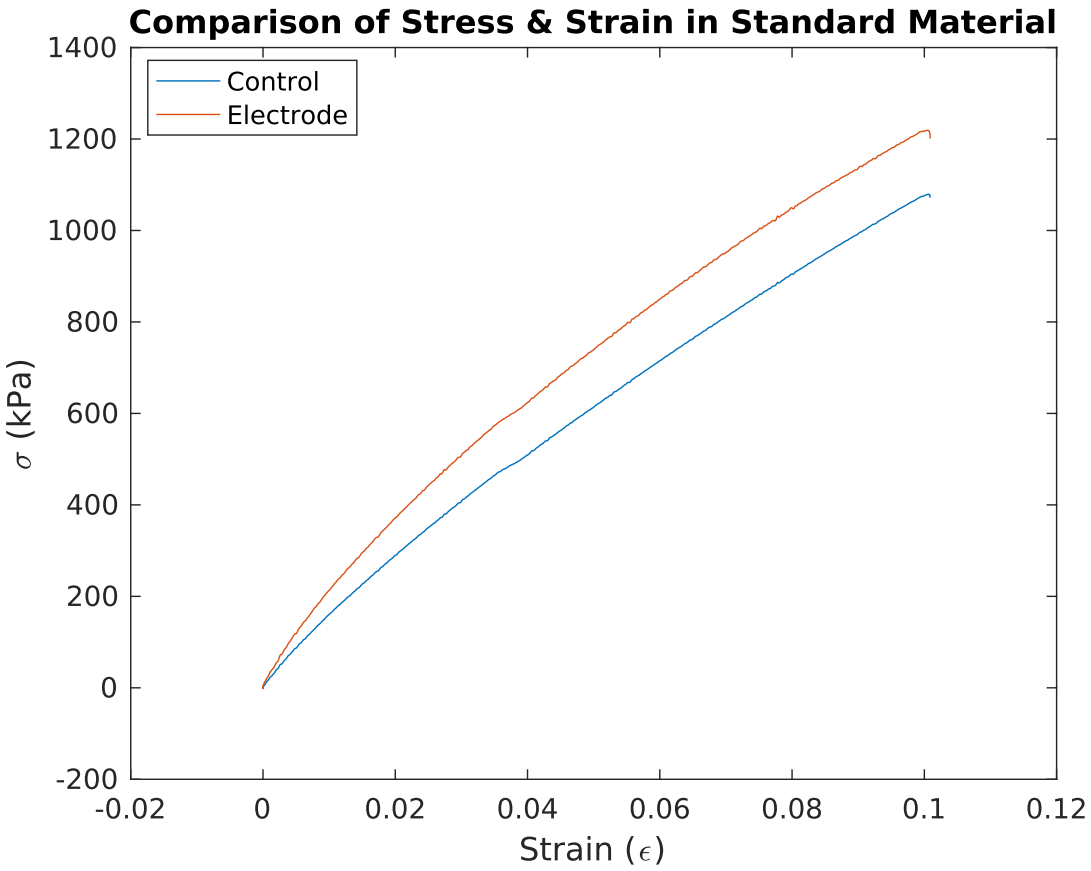

Fig. 3.3.: An example stress and strain comparison in a standard elastic material undergoing tensile testing.

3.3 Results of Tensile Testing of the Canine Vagus Nerve

The tensile testing procedures were done using the methods described in Section 3.1 for the canine vagus nerve. Figure 3.4 shows an example stress and strain curve comparison for the elastic test material with and without a cuff attached to it. Measurements for elastic modulus are made by estimating the slope of the curves in the initial toe region of the test. Table 3.1 summarizes the measurements made for the elastic modulus. Using a one-tailed Student's results in a significant difference at $p < 0.05$.

Table 3.1.: Summary of the modulus measurements of the nerve and nerve with cuff attached to it.

Nerve ID	**Nerve Modulus (kPa)**	**Nerve + Cuff Modulus (kPa)**
B70117	235.55	728.05
B70201	102.35	290.74
B70220	172.20	341.21
B70228	260.48	162.21
B70308	187.66	215.76
B70315	230.34	721.83
Mean	**198.10**	**409.97**
SD	**57.06**	**251.58**

Figure 3.4 shows the example stress and strain curves for the canine vagus nerve and the canine vagus nerve with a cuff electrode attached. The canine left vagus nerve and canine vagus nerve with cuff attached both stretched to approximately 10% strain without failure occurring and remaining elastic. The average elastic modulus for the canine left vagus nerve is 198.10 ± 57.06 kPa (n=6). The average elastic modulus for the canine left vagus nerve with a cuff attached is 409.97 ± 251.58 kPa (n=6).

Using a one-tailed Student's t-test gives a result of significance at a $p < 0.05$ for differences in the elastic modulus of each group.

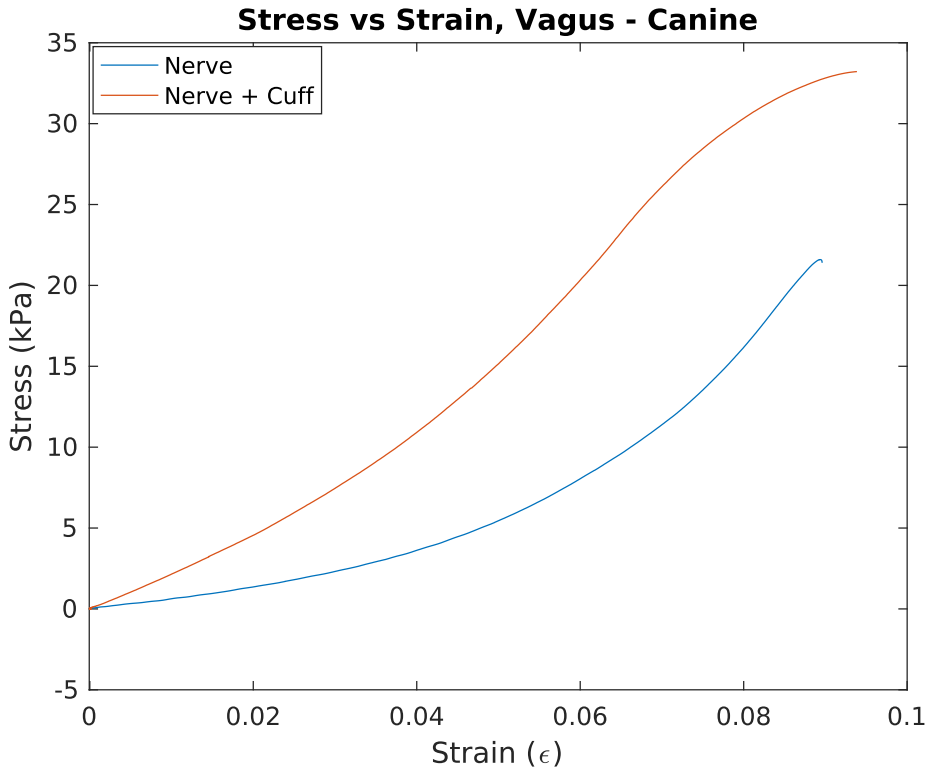

Fig. 3.4.: An example stress and strain comparison in a canine vagus nerve. The blue line indicates the stress and strain curve for the canine left vagus nerve, and the red line indicates the stress and strain curve for the canine left vagus nerve with a cuff attached to it.

3.4 Conclusions for Tensile Testing of the Canine Vagus Nerve

The attachment of the shape memory polymer cuff induces a variation of the stress and strain profile of the material in both a standard elastic material and a canine left vagus nerve according to the elastic modulus measurements in Table 3.1. However, a potential issue is that the testing environment to induce a 110% stretch is not the same as the 110% stretching that occurs in vivo. This is because experimentally it is

observed that upon excising the nervous tissue, it releases tension and shrinks. This is well visualized through the bands of Fontana [99], a natural strain relief mechanism. However, this shrinkage was not accounted for during tensile testing, and thus could skew the results. Figure 3.5 depicts the method of tensile testing. It is also visible in this figure that the clamping causes a boundary effect and could potentially skew results in unpredictable ways.

In addition to the attachment being less than realistic to chronic implant cases, one of the conclusions of Chapter 2 is that the reduction of strain for equivalent forces is in the region of the cuff. The analogous relationship of increased force or stress to reach equal strain for the whole material is apparent with an increased inherent modulus of the material, this whole material measurement does not fully capture the localized strain effects.

To address the strain locality and boundary effects, Chapter 4 synthesizes and adapts the FEM with imaging techniques to further characterize this relationship of strain reduction in the material region of the cuff attachment.

Fig. 3.5.: The fixture for tensile testing with a nerve fixed by alligator clips.

4. EX-VIVO EXAMINATION OF STRAIN ENVIRONMENT USING IMAGE PROCESSING

By examining soft tissue in mechanical testing, it is known that whole material properties are being measured. In many simplified geometries, assumptions can be made about the uniformity of the load distribution. Techniques such as digital image correlation have been developed to measure strain as a function of location in soft tissue. Zhou et al. [88] developed a speckle patterning technique to track the changes of small deformations in two dimensions of dissected aorta. Thompson et al. [89] developed a technique to measure localized strain in the region of a callus to predict loading outcomes using natural surface markers. A technique for measuring localized strain in uniaxial loading of soft tissue was developed as well by Doehring et al. [90] using the light deflecting properties of collagen. A similar technique is adapted in this chapter to make a low-cost strain imaging system.

By adding an implantable electrode to a nerve, the geometry of the testing environment becomes more complex, and it becomes necessary to examine the effects of the electrode on the localized tissue strain environment. The use of sophisticated imaging techniques will allow for a better understanding of the localized effects and influence of the material properties of the electrode. In this chapter, an imaging and post-hoc strain tracking technique is developed by applying markers to the nerve surface using an inkjet printer and freezer paper. This strain tracking technique is compared to a finite element model developed to imitate the tensile testing environment and partial attachment of the cuff electrode to the nerve. Observations are made about the stress conditions of the nerve and solutions are proposed and modeled to solve an identified potential mechanism for a fibrotic encapsulation conducive environment.

4.1 Methods

4.1.1 Methods For Mechanical Tensile Testing

The canine vagus nerve sections are excised after euthanasia according to the standards of the Indiana University (IU) Laboratory Animal Research Center (LARC) and stored in a phosphate-buffered saline solution for no more than two hours before tensile testing occurs. Testing occurs at a room temperature of 22°C.

To test the materials, the ends of the nerve were fixed using alligator clips that have been soldered to Luer Lock needles that fit onto prefabricated test fixtures. For each material, the diameter of the approximately cylindrical objects were measured using a caliper and recorded to make area computations for use in analysis. The length between the fixation points were measured as the initial length of the material to convert displacement to strain during analysis. Attaching the shape memory polymer cuff to the materials required heating the cuff in a warm bath of 50°C for 5 minutes before applying it the material. The edge of the materials received a light application of super glue (Loctite® 414™ Super Bonder®) using a hypodermic needle to apply the no-slip condition of the cuff. For the imaging tests, the cuff was applied to only half of the nerve on the non-imaging surface of the nerve.

According to the works of Fung [81], the first three cycles of loading will have the largest changes in viscoelastic response, but after this there should be minimal change indefinitely for cycles. Following this understanding, the nerves were cyclically loaded 5 times to the same stretched length before the measured loading is analyzed. The materials were stretched at a rate of 0.5 mm/s to a designated length. Data were extracted and analyzed in MATLAB® R2016b to measure the slope of the stress-strain curve for the elastic modulus.

The tensile and mechanical testing system is a custom-built system, created by Drs. Ken Yoshida and Winnie Jensen [98]. The Vitrodyne V1000 system performs the tensile or compression actions, which is controlled by the JVL DMC10 controller. The Sensotec Model 31 load cell interprets the force and the SG010 strain gauge

amplifier sends that signal to the National Instruments (NI) ® BNC 2111 data acquisition board. The Vitrodyne V1000 and the NI BNC 2111 data acquisition system communicate and synchronize with a Dell® Optiplex computer. Figure 3.1 shows a simple schematic with data flow indicated by the arrows.

4.1.2 Tracking Strain Using Digital Image Correlation

The tracking of stress and strain using digital image correlation has been done in other applications using complex techniques such as speckle patterning [88] with spray paint materials and imaging modes like quantum fluorescent dots and collagenous light diffraction [90]. This chapter develops a low cost technique for creating digital image markers for tracking displacement using an inkjet printer and plastic coated freezer paper. The printer uses a 'wet' ink deposition that quickly dries and evaporates on standard printing paper. By attaching the freezer paper to normal paper and depositing the wet ink on the plastic coated surface, the wet ink does not dry as quickly and can be transferred to moist surfaces. By creating a thinly printed array of markers and transferring it to the surface of the nerve, a low cost method for tracking movement on biological surfaces can be developed with an image processing algorithm.

The primary tool used for identification of the markers in image processing is the Hough transform [100]. It is a common feature recognition tool used in digital image processing to extract information and desired characteristics [101]. It generally is able to do this by finding imperfect instances of objects within tolerances and classes of objects based on the formulation given. To perform the circular Hough transform for fast recognition of circular objects, the image is processed using a binarization technique to convert from a color image to a black and white image. The use of different thresholding techniques will vary from sample to sample based on the needs of the image segmentation due to contrast, brightness, and variation in color [102].

For this method, the built-in localized gray thresholding technique by MATLAB® was used.

$$(i-a)^2 + (j-b)^2 = r^2 \tag{4.1}$$

Equation 4.1 details the fundamental operator for identification of the circular objects found using the circular Hough transform. Every pixel of an image is binned into a cell labeled a with a value set to zero. Next, every possible edge point, labeled i and j, are found using the Sobel edge detection method [103]. If a pixel a that is within a boundary edge of points (i, j), it is considered a potential circular center point, and all values of b are then found to satisfy Equation 4.1 and identified as the center points of circles. The Sobel edge detection method solves for the detected edges from its magnitude combined components G_x and G_y as noted in Equation 4.2.

$$G = \sqrt{(G_x)^2 + (G_y)^2} \tag{4.2}$$

The Sobel equation is found by convolving the source binary image, A, with two neighbor matrices, G_x and G_y, to determine edge location. The x and y components of the neighbor matrix convolution steps are equations 4.3 and 4.4 respectively where the resulting matrices indicate points where an edge occurs when the magnitude of G is below a threshold. The MATLAB® default threshold for neighbor matrix convolution is a value of 3 for any cell. This method is common in digital image processing for segmentation in many applications for its robust feature identification ability.

$$G_x = \begin{pmatrix} 1 & 0 & -1 \\ 2 & 0 & 2 \\ 1 & 0 & -1 \end{pmatrix} * A \tag{4.3}$$

$$G_y = \begin{pmatrix} 1 & 2 & 1 \\ 0 & 0 & 0 \\ -1 & -2 & -1 \end{pmatrix} * A \tag{4.4}$$

Once the centers of all circles in the image are found, they are ordered lengthwise from the base along the central axis of the nerve. A region of interest selection is performed graphically to exclude any circles that are not of interest or have been erroneously selected.

To utilize this method of marker tracking, videos are recorded using a Canon® EOS M3 camera attached to a microscope while the nerve underwent tension. The strain is tracked by calculating the difference of lengths between the center of the circular markers in each frame, divided by the initial length between each segment. Each frame of the video is extracted as the time sampling frequency at 60 frames per second. Tensile testing is performed following the conditions described in Section 4.1.1. Figure 4.1 details the algorithm procedure where each frame has a region of interest selected, the Hough transform identifies circles on the surface of the nerve, and the circular centroid locations are saved before strain is calculated.

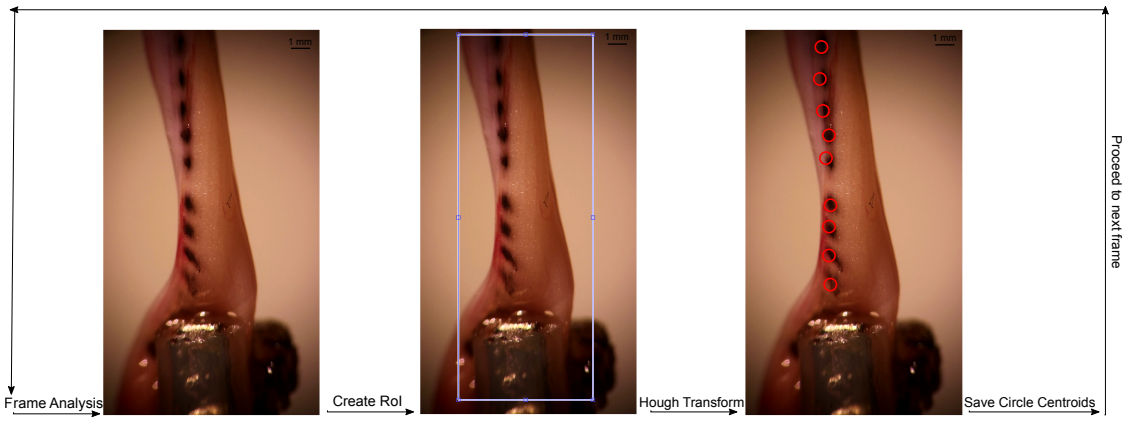

Fig. 4.1.: The algorithm process for extracting frames, selecting a region of interest, and performing the Hough transform to identify the locations of the centroids of the circular markers on the surface of the nerve, and then saves the location of the centroids before proceeding to the next frame in the video.

4.1.3 Development of the Finite Element Model of the Testing Condition

The creation of the FEM is dependent on the geometric fidelity of the model. In this chapter, iterations of a FEM were developed to compare the strain of the central axis and the surface in axial tension as well as exploring the variation in boundary conditions and nerve length dependence. An extraneural half cuff was modeled and fit to the surface of the nerve to evaluate the strain environment upon axial loading of the nerve. This cuff was meant to simulate the more realistic geometry where only half of the cuff was attached and in contact with the nerve and to account for the testing conditions to see the surface markers during tensile testing. The nerve was given a modulus of 500 kPa and a Poisson ratio of 0.4. The cuff was based off a SMP electrode and was given a modulus of 5 MPa with a Poisson ratio of 0.3. Its dimensions were 7 mm in length, 100 μm thick, and fit the circumference of the nerve perfectly with half of the cuff being removed from the geometry in models that have ideal attachment. In conditions that more realistically interpret the tensile test, the nerve was 15 mm in length and the cuff was 5 mm in length.

The nerve was pulled in tension at each end with a 70 mN/1.5 mm^2 load for the ideal loading condition. To match the loading of the mechanical tests, the nerve was fixed at one end and pulled to approximately 110% of its initial length. The cuff was attached to the nerve with two no-slip boundary conditions where the inner diameter edge of the cuff is perfectly and rigidly attached to the nerve. This was seen as an ideal attachment case where the cuff was touching the nerve but there is no slipping at either end of the cuff and could ideally by achieved *in vivo* using sutures, surgical glue, or any other number of applications.

During the tensile mechanical tests and the digital image correlation for strain tracking, the surface level axial strain was being approximated on the surface opposite the cuff attachment. To further develop this relationship, both the central axis axial strain and the surface level axial strain were extracted from the nerve FEM to observe their relationship.

4.2 Results of Digital Image Correlation in Tensile Testing

A custom MATLAB® code was used to plot data to visualize strain as a function of both time and length. Location normalization is done to reduce the redundancy of markers maintaining close proximity to each other and to make comparison between measured nerves of different length. Figure 4.2 and Figure 4.3 are results of testing two segments of the same nerve in tension: one test composed of just the nerve in tension and the other composed of the nerve with a cuff attached in tension.

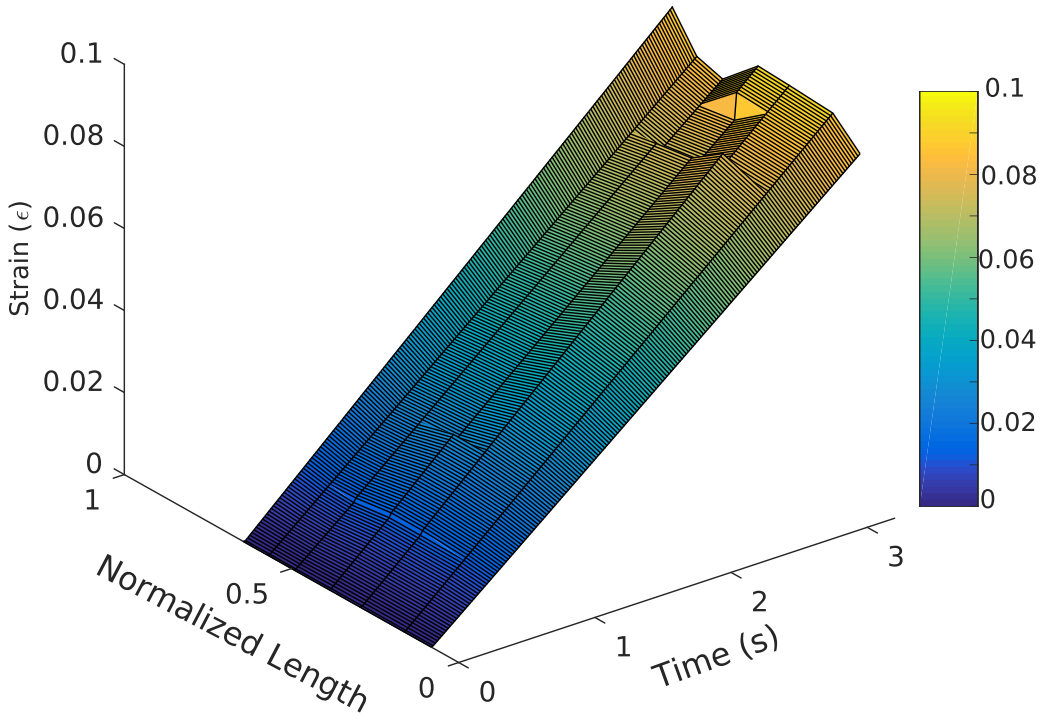

Fig. 4.2.: The plot of strain as a function of time and length as a surface plot in the canine vagus nerve during axial tension with digital image correlation techniques used to track the markers along the length of the nerve. Lengths are normalized to their initial length to make comparisons between measurements.

Figure 4.3 depicts the surface plot of strain in a nerve with a half cuff attached to it as a function of length and time. Noticeably, the axial strain functions nearly linear as a function of time for each length segment, but the axial strain functions non-linearly as a function of length for both Figure 4.2 and Figure 4.3. Figure 4.4 shows the initial frame for the experiment resulting in the data for Figure 4.3 where the half cuff is attached to the back of the nerve in approximately the middle third region (normalized length 0.3-0.6) of the canine vagus nerve.

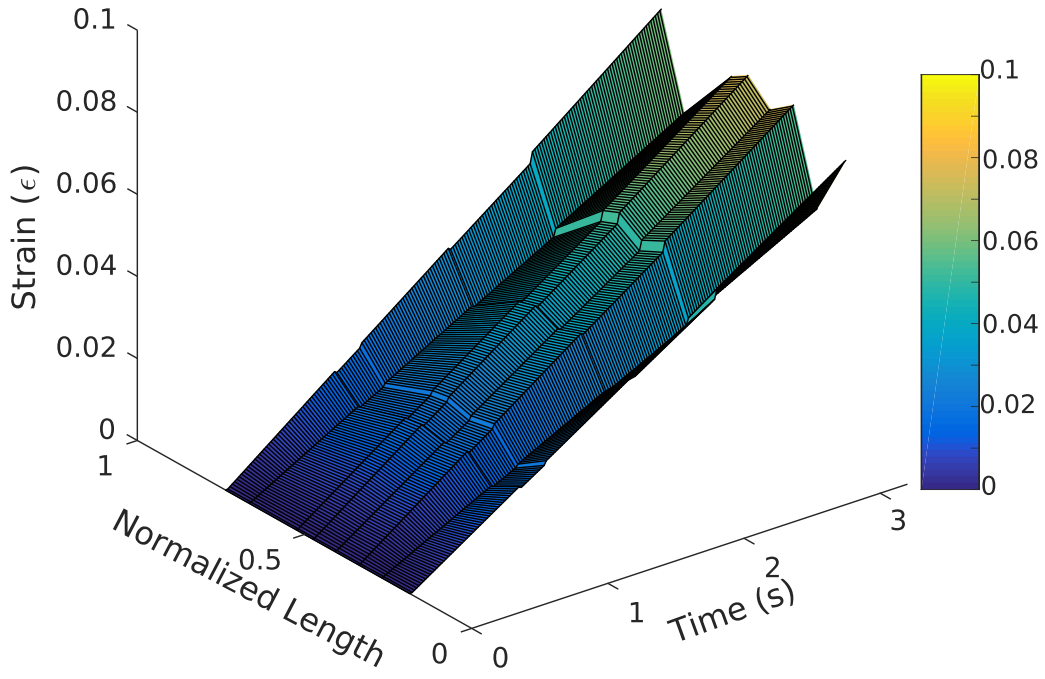

Fig. 4.3.: The plot of strain as a function of time and length as a surface plot in the canine vagus nerve with a half cuff attachment during axial tension with digital image correlation techniques used to track the markers along the length of the nerve. Lengths are normalized to their initial length to make comparisons between measurements.

Fig. 4.4.: Image of the first frame of the tensile tests in the canine vagus nerve with an attached cuff and digital image correlation markers to show the location of the cuff.

In comparing Figure 4.2 and Figure 4.3 it is clear that there is a substantial difference in the axial strain dependence of the nerve and the nerve with a cuff attached that is primarily visible near the attachment points of the cuff on the nerve. To further understand the relationship, one can examine the compliance of the nerve as a function of length and time. Figure 4.5 and Figure 4.6 depict a compliance approximation of the two previous tests as functions of length and time by dividing the strain functions by the measured force during tensile testing. The compliance of the nerve remains relatively constant with periodic variations where the values increase rapidly and immediately decrease.

It is not abundantly clear why the compliance of the nerve and nerve with cuff attachment indicate variations in compliance change over time but a mechanism may

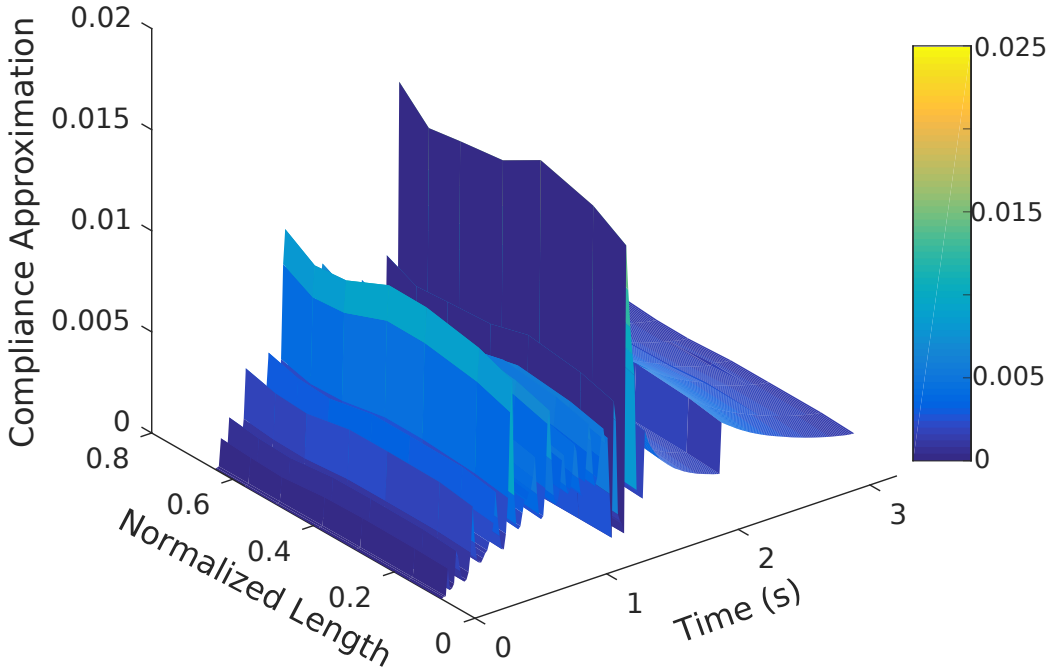

Fig. 4.5.: A plot of the compliance approximation of the nerve during tensile testing as as a function of length of the nerve and time in tensile testing.

involve the organizational structuring of the nerve. Axons of various length in the nerve are not aligned coaxially with the nerve, but rather are in a continuous 'snaking' pattern. In tensile testing, the sudden cyclic changes in compliance may be a result of these axons unfurling and beginning to bear load or possibly even failing. The exploration of this mechanism may require significant method changes, but could possibly raise important questions about the functions of axons in realistic load bearing. To further examine the strain relationship between the measured surface axial strain and the axial strain at the center of the nerve, a finite element model was developed in Section 4.3 and compared to the measured surface strain.

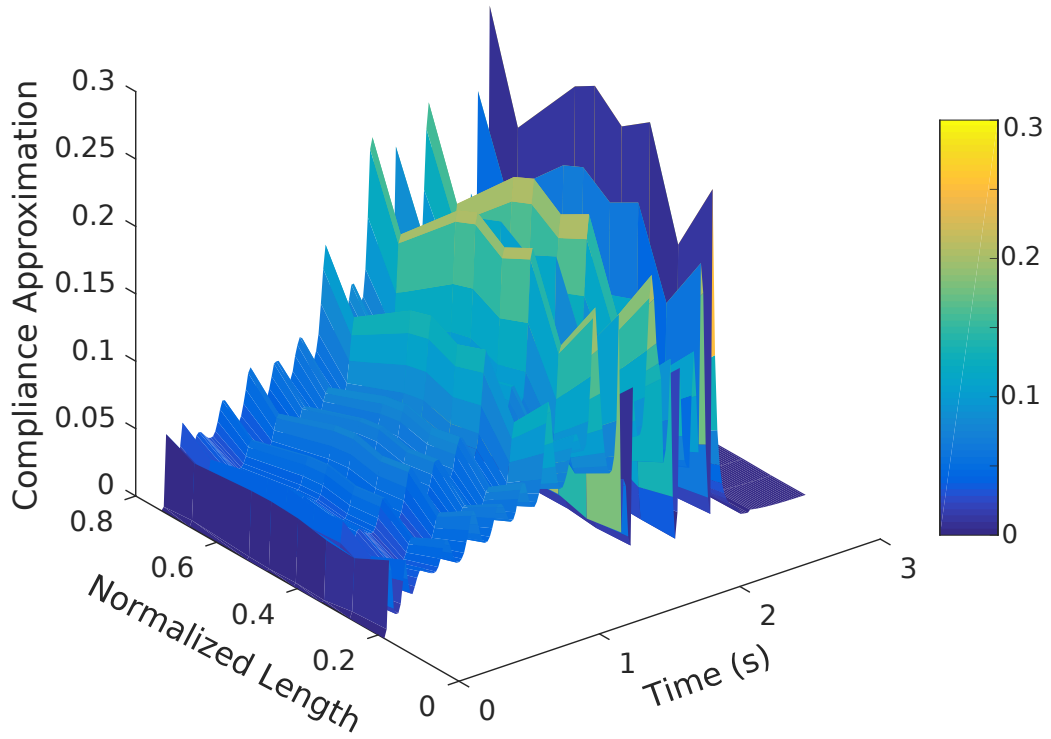

Fig. 4.6.: A plot of the compliance approximation of the nerve with a cuff attached during tensile testing as as a function of length of the nerve and time in tensile testing.

4.3 Results of Finite Element Modeling of the Testing Condition

The finite element model development in conjunction with the digital image correlation results in a number of scenarios to examine. It is important to examine a FEM where the conditions remove boundary effects and simply examine fundamental interactions, but it is also important to use a realistic, experimentally based design to compare the two analysis methods.

Figure 4.7 summarizes the result of the longer nerve FEM with axial strain displayed with the color map. A notable difference between the half cuff model and the

full cuff model, as discussed in Chapter 2, is the development of a bulge in the cuff region. A potential reason for this is detailed in Figure 4.8 where the shear stress streamline is plotted, showing that the shear stress deflects away from the cuff as it approaches the center of the nerve as its mechanism for reducing strain.

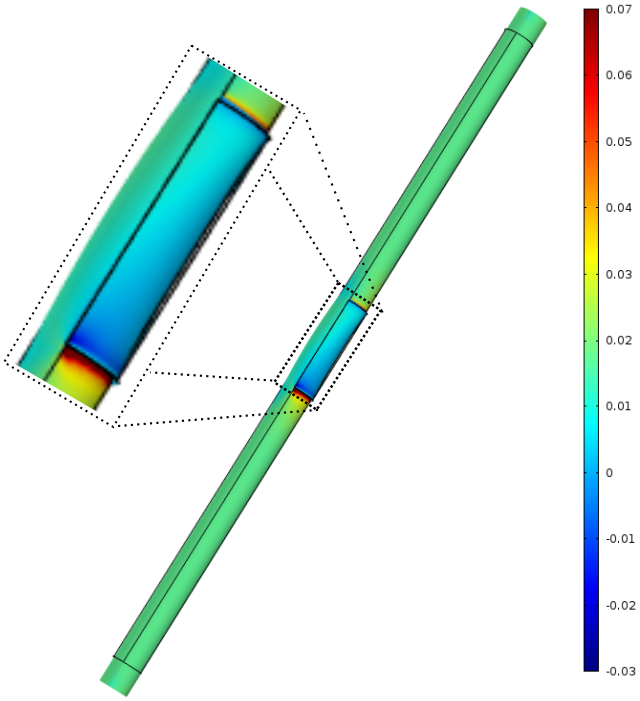

Fig. 4.7.: Finite Element Analysis results of the model with axial strain plotted with the color map. The nerve is 50 mm in length and the cuff is 7 mm length with mechanical properties described in section 4.1.3.

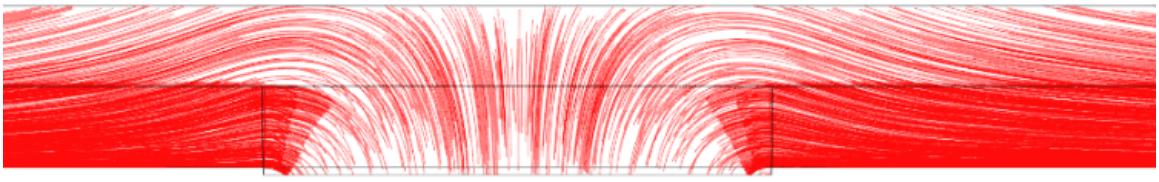

Fig. 4.8.: Plot of the shear stress flow through the nerve as it approaches the half cuff region and causes a bulge in the deformation of the nerve.

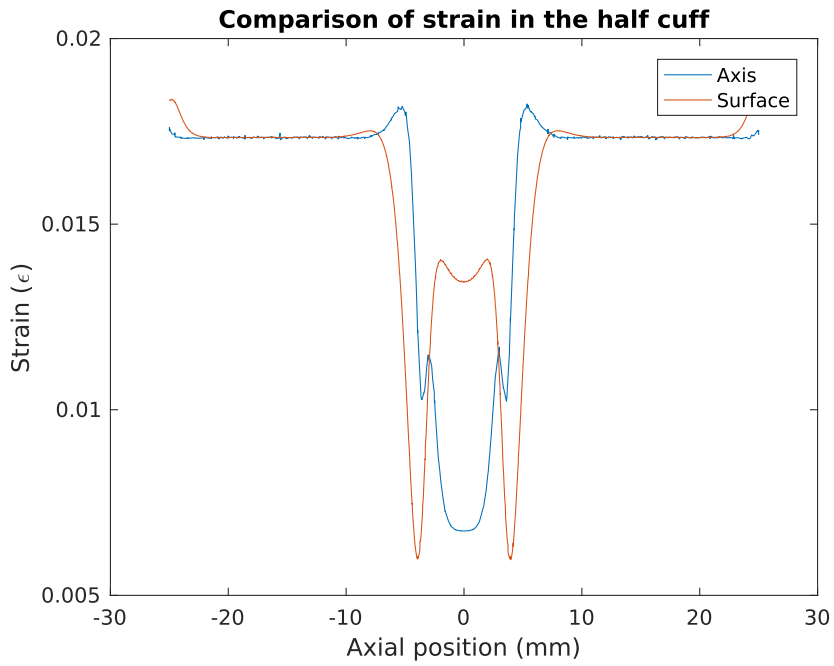

Fig. 4.9.: Comparison of axial strain at the central axis and at the surface of the nerve from the finite element bulk nerve model.

Another way of examining this bulge development is to examine the axial strain at the surface and the axis of the nerve. Figure 4.9 examines this by showing that surface strain reduces in the region of the cuff but is more than ten times larger than at the axis. This difference is due to the rapid change in principal planes from the boundary conditions of the cuff and the shear stress flow as depicted in Figure 4.8.

Moving forward, it is important to know if this strain relationship, as characterized, is real and comparable to the measures made in Section 4.1.2. To do this, the half cuff model's nerve was truncated to 15 mm, and the cuff length was 5 mm. The results of the axial strain in the half cuff model are extracted and compared to the measured results. Figure 4.10 depicts the FEA results of the model where the previously seen bulge is still prevalent but a flexing of the cuff is more noticeable.

To compare the strain at the surface between the FEM and the digital image correlation system, the values are plotted against one another. Unlike in the FEM,

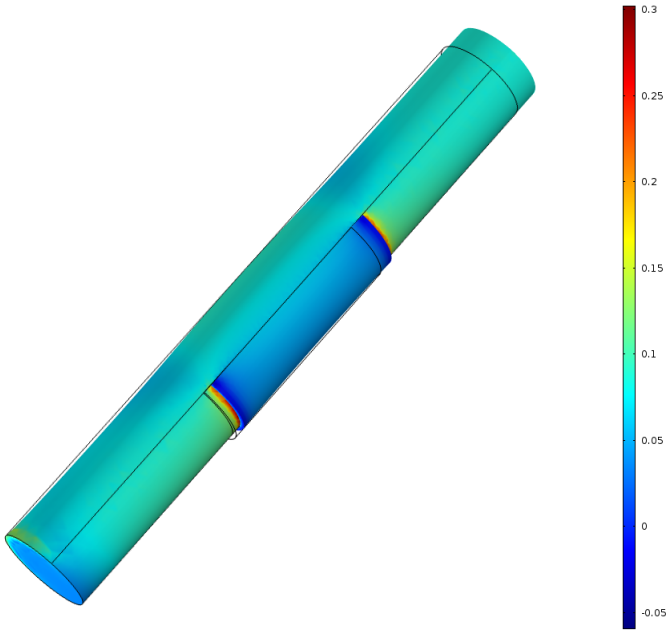

Fig. 4.10.: Finite Element Analysis results of the model with axial strain plotted with the color map. The nerve is 15 mm in length and the cuff is 5 mm length with mechanical properties described in section 4.1.3.

the placement of the half cuff is not perfectly symmetrical. To more standardize the comparison, the length segments are normalized as multiples of cuff length and centered around 1.5 cuff lengths as each test is approximately 15 mm in length when the nerve is attached. For comparing the FEM when there is no cuff attached, the experiments are normalized by nerve length to best compare the data sets. This will correct some of the variation due to technique and allow for a Pearson's R correlation coefficient calculation to be a better measure for relation.

Figure 4.11 shows the comparison of strain between the FEM and 4 measured strain curves from the digital image correlation system with the nerve. Pearson's R correlation coefficient is calculated for the curves and results in an average value of -.1371 $\pm$ .2042. While this shows that there is a difficult correlation in data shape,

the error associated with the measurements was an average of 2.76% ± .7892% so it is considered acceptable.

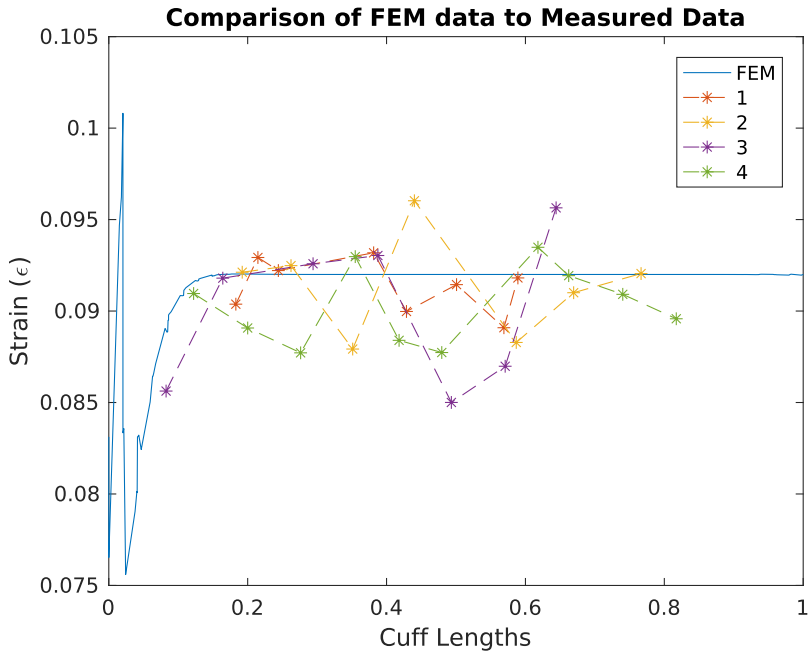

Fig. 4.11.: Plot of the comparison of FEM data of axial strain at the surface of the nerve when normalized to nerve length.

Figure 4.12 shows the comparison of strain between the FEM and 4 measured strain curves from the digital image correlation system with the nerve and a cuff attached. Pearson's R correlation coefficient is calculated for the curves and results in an average value of .8574 ± .0481. It is important to also consider that the surface spatial resolution of the FEM is close to 700 points and the digital image correlation system uses between 8 and 12 points for measurement.

To continue with comparing the data sets, it is appropriate to examine their relation when the FEM has a similar spatial sampling rate. To do this, the sampling rate of the FEM is considered to be sampled at a rate of 40 $k\xi$ where 1 ξ is 1 sample/meter. The sampling rate of the digital image correlation system is then approximately 500 ξ. The data of the FEM is filtered using a simple 4th order low-

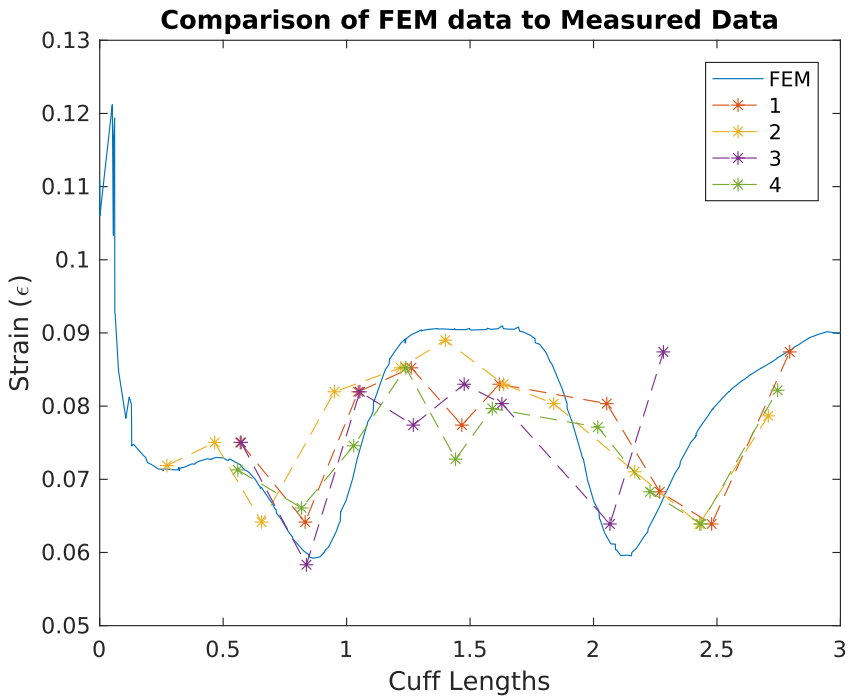

Fig. 4.12.: Plot of the comparison of FEM data of axial strain at the surface of the nerve with cuff attached and when normalized to cuff lengths and centered around 1.5 cuff lengths.

pass filter at 500 ξ and then decimated to more closely and accurately represent the sampling rate of the digital image correlation system.

Figure 4.14 shows the comparison of strain between the filtered and decimated data of the FEM and the measured data from the digital image correlation system. Pearson's R correlation coefficient is calculated for the curves and results in an average value of .5941 $\pm$ .1679. This indicates that the digital image correlation system is sufficiently capable of predicting the behavior of the FEM. This relationship would indicate that the bulging seen in Figure 4.8 is indeed a real event. Section 4.4 discusses why this bulge may be a problem and proposes solutions to design cuffs around this event.

Figure 4.13 shows the comparison of strain between the FEM and its own filtered and decimated data. Pearson's R correlation coefficient is calculated for the curves

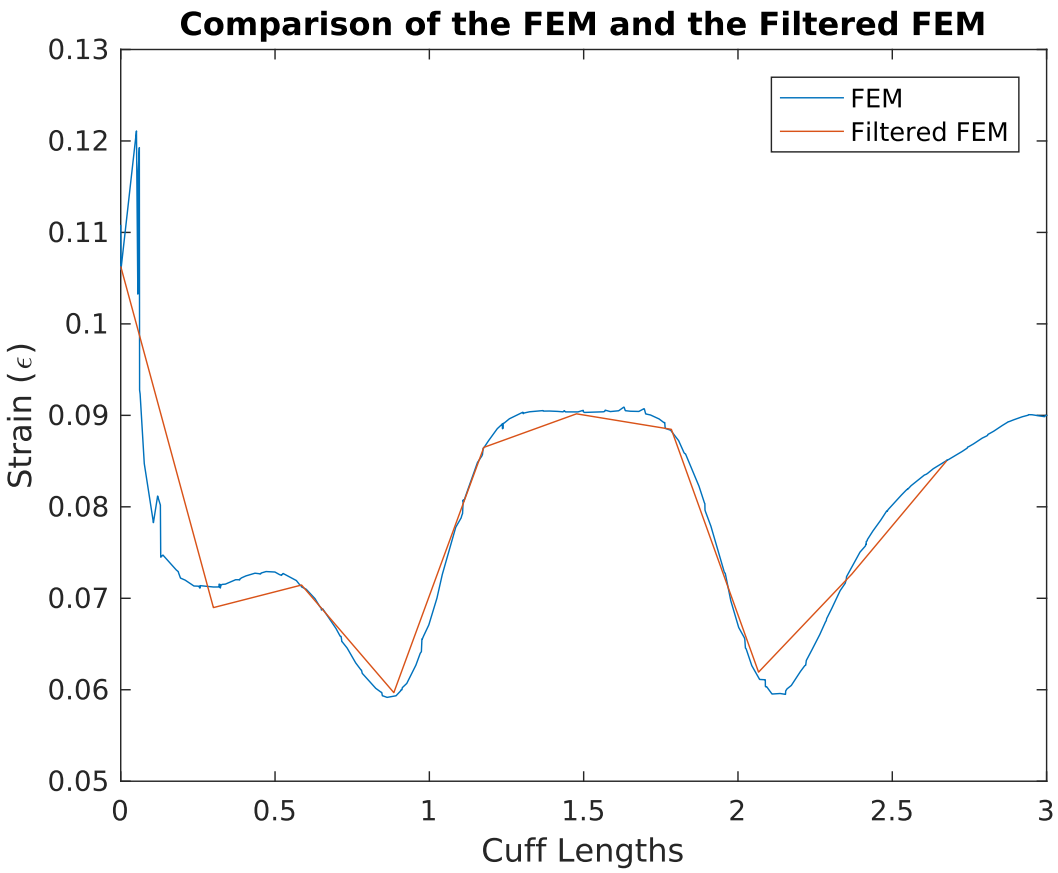

Fig. 4.13.: Comparison of the FEM with its own filtered and decimated data set after being filtered at 500 Hz and decimated to 10 samples.

and results in a value of .9873. This indicates that simple digital filtering without the introduction of noise causes a non-insignificant difference in the measured strain function along the length of the nerve.

Another way to visualize the comparison of the predicted strain and the measured strain is to plot the strains as a function of one or the other. By plotting the measured values as a function of the predicted values it can be observed in Figure 4.15 that the values closely follow a line with a slope of one. In Figure 4.15(a) the plot shows a small range of steady state error around the predicted strain value.

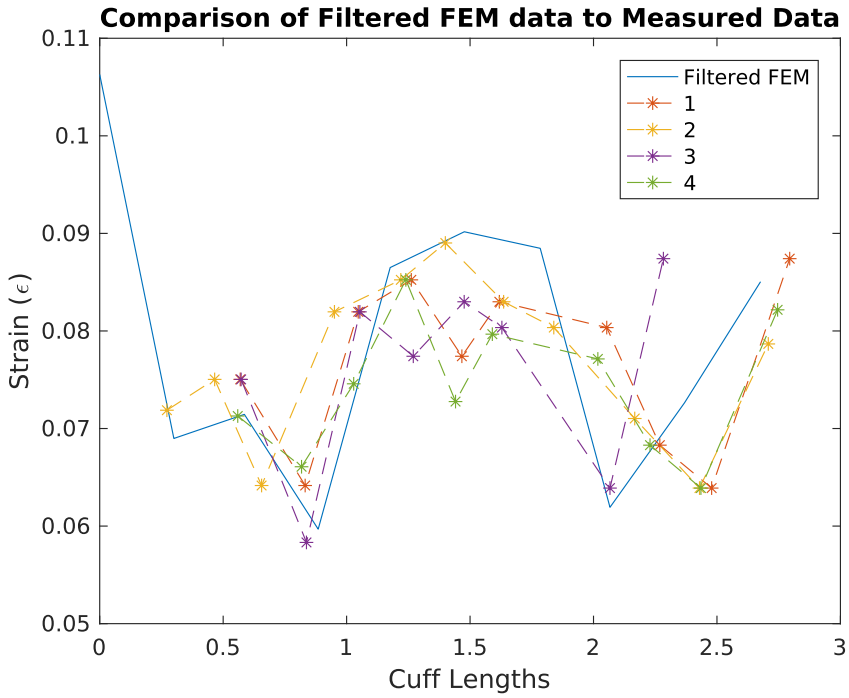

Fig. 4.14.: Comparison of the FEM data decimated and filtered at 500 Hz to the measured data of the digital image correlation system

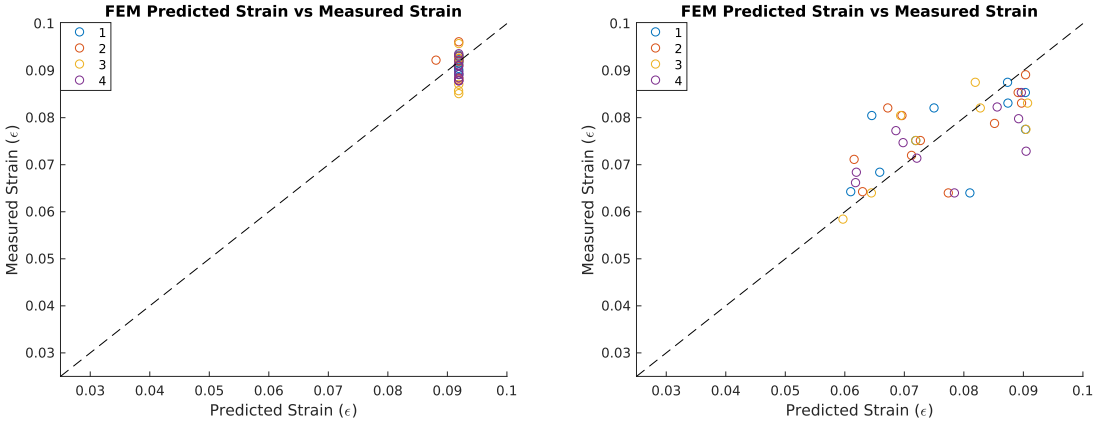

(a) Nerve

(b) Nerve with Half Cuff

Fig. 4.15.: Plots of the measured strain values as a function of the predicted FEM values with a comparison to a line with a slope of 1.

4.4 Proposed Solutions and Designs for New Cuff Electrodes

An important observation from Section 4.3 is the bulge that occurs in Figure 4.7 and Figure 4.10 in the region of the half cuff. According to simple principles of cellular mechanotransduction [104], stretch is a primary mechanical signal for cellular signaling. Epithelial cells in the body are well known to recruit macrophages and induce fibrotic tissue deposition [105]. Such a mechanism may be responsible for the continuous fibrotic encapsulation. A potential way to reduce this bulging caused the shear flow, as seen in Figure 4.8, is to maintain the stiffness in the axial direction, but allow for radial stretch so that the shear flow more regularly flows through nerve without deflecting away from the attachment points. To do this, a simple design would be to make a two phase cuff, where there are stiff axial bars and a very pliable medium acting as the primary medium of the cuff. Figure 4.16 details the simple FEM that is developed where 9 equally spaced 50 MPa, .1 mm diameter bars reinforce a 500 kPa, 200 micron thick half cuff that encompasses a nerve with a no-slip condition at the binding edges.

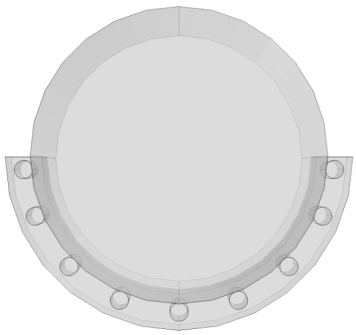

Fig. 4.16.: Depiction of the simple FEM that is developed where 9 equally spaced 50 MPa, .1 mm diameter bars reinforce a 500 kPa, 200 micron thick half cuff that encompasses a nerve with a no-slip condition at the binding edges.

By applying the same load as the model in Figure 4.7 an appropriate comparison between the models can be made. Figure 4.17 details the result of the FEM with the nerve and new cuff design simulated. Noticeably there is a distinct lack of visible bulging in the cuff region.

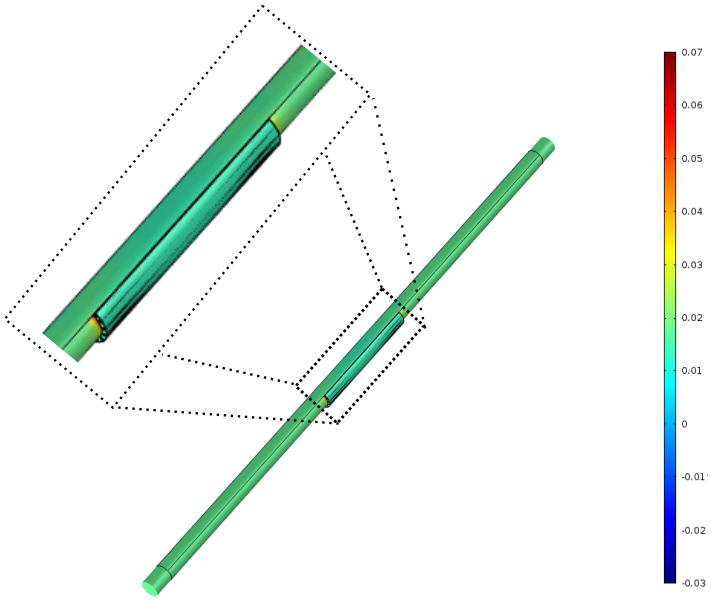

Fig. 4.17.: Finite Element Analysis results of the nerve and reinforced cuff with axial strain plotted with the color map.

Figure 4.18 shows the comparison of axial strain at the surface and the axis in the new reinforced cuff design. The strain values are very close with minor differences. This would indicate the reinforced bars are bearing the load and the cuff is allowed to stretch circumferentially evenly to reduce bulging.

By comparison, Figure 4.19 shows the surface axial strain in the reinforced cuff model and the regular half cuff model. The strain values in the region outside of the cuff are the same and the inner cuff region strain is distinctly different, showing that the reinforced model has a change in the shear stress environment which is validated by examining the displacement flow of the model in Figure 4.20.

In Figure 4.20, the displacement direction more regularly directs itself to the cuff without the induction of a bulge. The direction of the strain the cuff by shear stress

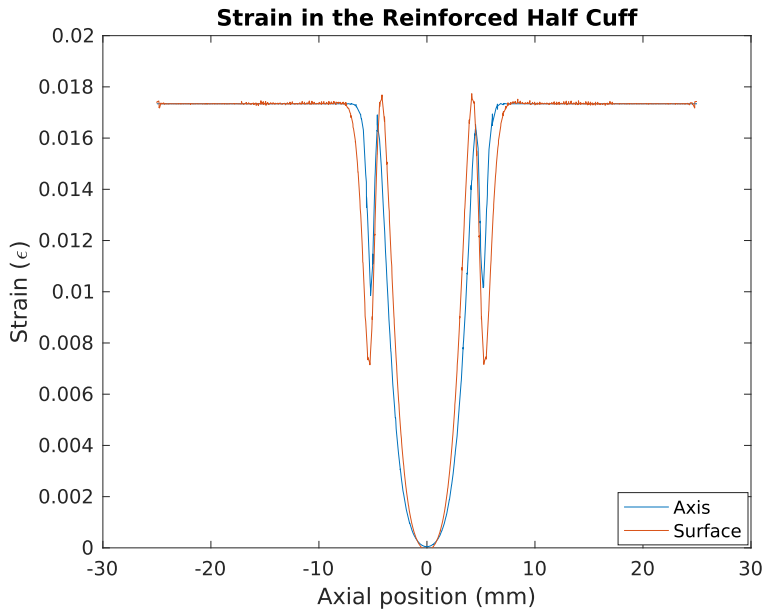

Fig. 4.18.: Comparison of axial strain at the surface and central axis of the nerve with the reinforced half cuff attached to the nerve.

direction change could possibly be an issue. Another potential method for this is to reduce the surface area of contact of the no-slip by changing the geometry of the cuff edges with holes, ruffles, or other boundary changes. This modulation of the attachment area is a novel idea in electrode design.

4.5 Conclusions of the FEM and Digital Image Correlation System

To summarize, the strain location dependence seen in the finite element model is validated with the digital image correlation system that is developed to use the Hough transform for circular region recognition using a low cost ink transfer method. This is validated by comparing the measured strains in a modified FEM that closely resembles the test environment and comparing the results to the measured data of the digital image correlation system.

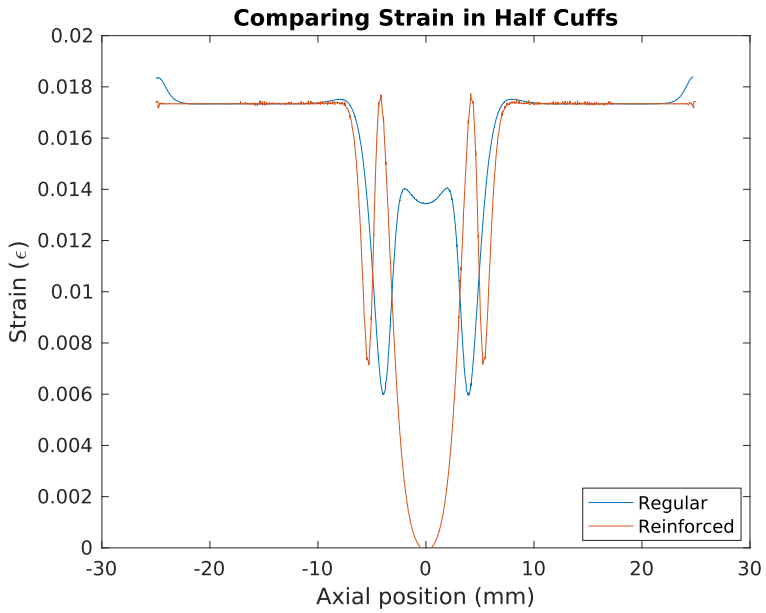

Fig. 4.19.: Comparison of the surface axial strain in the half cuff and the reinforced half cuff where the nerve region outside of the cuff experiences the same strain in each model but is significantly within the cuff regions.

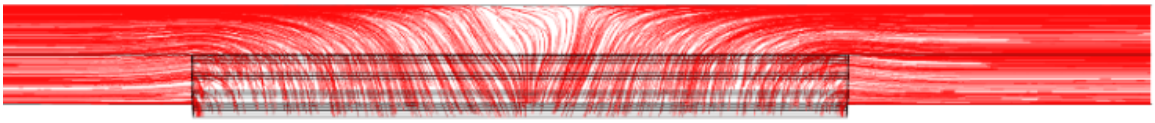

Fig. 4.20.: Plot of the shear stress flow as it approaches the reinforced half cuff region and evenly distributes through the nerve without bulge induction.

The digital image correlation system's measured values are compared using Pearson's correlation coefficient showing that they are significantly related to their predicted data and different from each other. The predicted values matching the measured value indicates that the bulging phenomenon is a possibly real mechanism that may be driving mechanotransduction cellular signaling to modulate the chronic encapsulation of the electrodes causing failure.

A design method and example is proposed to continue reinforcing the axis of the cuff for stability while allowing the cuff to expand radially to prevent bulge formation as seen in the shear flow streamlines in Figure 4.8 and corrected in Figure 4.20. Potential other mechanisms for reducing this shear change altogether may involve modulating the boundary edges of the cuff to reduce the no-slip contact area to modulate the formation of anti-clastic stresses that form.

4.5.1 Extended Comparisons with the Laminar and Bulk Model

The primary model in use in this work is the bulk nerve model which may be exaggerating some effects due to the homogeneous material property. The results of the study showed interesting modulation of the boundary effects and an identifiable relationship between the surface and axial strain of the nerve. Further comparisons become necessary when considering the effects of the laminar and bulk model, as well as the effects of the reinforced. As a continuation of the analysis, models that compare a bulk and laminar nerve with a full, reinforced cuff and a shortened nerve with a half cuff are developed using the same properties as described in Section 2.1 and Section 4.1.3.

The full, reinforced cuff has the same properties as the cuff designed in Section 4.4 but it is a fully circumferentially attached cuff with sixteen equally spaced reinforcement bars.

Figure 4.21 shows the results of the FEA with the bulk nerve and reinforced model. There is consistent strain in the nerve and cuff region with stress concentrators at the cuff attachments. Figure 4.22 shows the results of the FEA with laminar nerve and shows that there are similar effects but a slight difference of strain values in the nerve and cuff regions with increased strain at ends of the nerve where loading is applied.

To further compare the models, plotting the axial strain as a function of length shows that there are distinct differences between how the models experience strain through attachment of the cuff. Figure 4.23 shows that there are differences at the

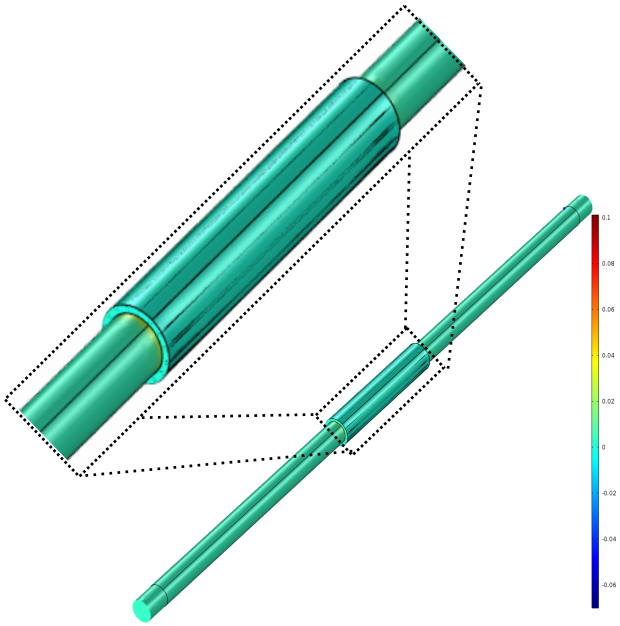

Fig. 4.21.: Results of the finite element analysis of the bulk nerve with a full, reinforced cuff in tension and plotted with a color map of axial strain.

loading points where the laminar model experiences a great boundary effect. There are also major differences at the cuff attachment point where the bulk model sees a very large formation of the anti-clastic forces and the laminar model does not see the same effect. This may be a result of the perineurium membrane reducing the transmission of the boundary effects between the epineurium and endoneurium.

To further compare this anti-clastic stress formation, the displacement flow streamlines aid in visualizing this effect. Figure 4.24 shows these streamlines in the bulk and laminar nerve models. In the bulk nerve model, the streamlines congest and disperse in an uneven pattern throughout the cuff region. In the laminar nerve model, the streamlines flow evenly and disperse in the cuff region. This even dispersement shows that the strain is being more evenly distributed and that the cuff is able to more effectively bear the load.

The results of both Figure 4.23 and Figure 4.24 indicate that the anti-clastic strain is much less pronounced in the laminar model due to the attachment of the cuff to

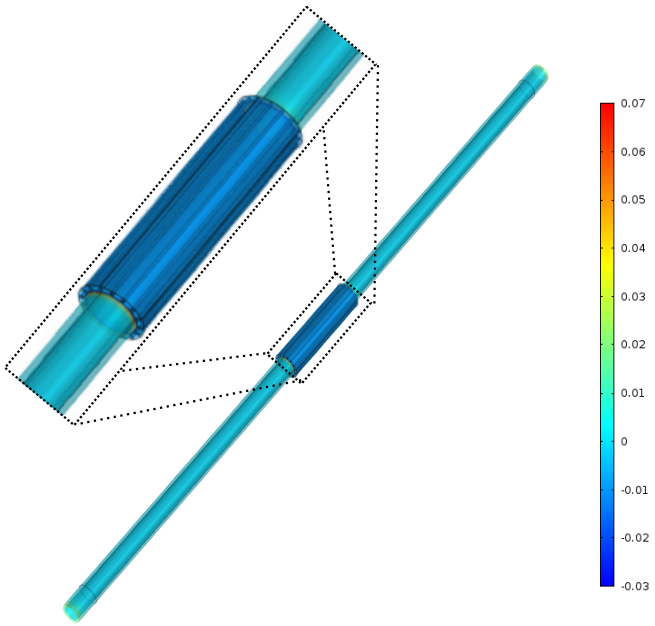

Fig. 4.22.: Results of the finite element analysis of the laminar nerve with a full, reinforced cuff in tension and plotted with a color map of axial strain.

the epineurium and the perineurium preventing the transmission of the boundary effects to the epineurium and the central axis of the nerve. To further understand this relationship, a continued comparison with half cuff model is made.

The laminar nerve with a half cuff is developed with the same methods as Section 4.1.3 but the nerve model is from the properties of the laminar nerve in Section 2.1. The comparisons of axial strain at the surface and the central axis are made to see the differences as well as to identify the formation of anti-clastic stresses from the electrode attachment.

Figure 4.25 shows the FEA results of the shortened laminar nerve with a half cuff attached. It is fixed in displacement at one end and pulled to approximately 110% of its original length by the other. Again, this method more closely reflects the real testing conditions in the digital strain tracking system. As expected, a bulge forms in the nerve and there are stress concentrators around the attachment points of the half cuff.

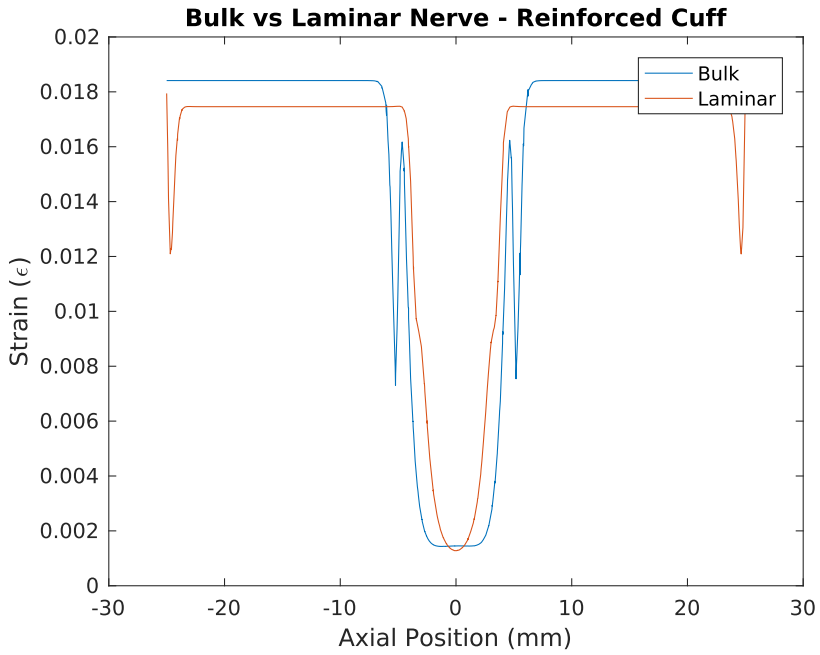

Fig. 4.23.: Comparison of the central axial strain in the bulk and laminar models with a full, reinforced cuff attached by plotting as a function of length of the nerve.

To continue the analysis, the laminar short nerve is examined to compare the surface and axial strain. The trend of Figure 4.26 is similar to the bulk nerve's comparison of the central axis and surface strain where there is a disparity in the strain before the cuff region and in the cuff region as well. An observation is that the laminar model is able to reach a steady state strain value before the cuff region both the surface and central axis, unlike the bulk model which was only able to reach the steady state strain the central axis strain. While this indicates there is still significant anti-clastic stress, there are some differences already present in the model. These differences are further explored by examining the differences directly.

Comparing the behavior of the bulk and laminar model at the surface for axial strain in the half cuff shows an immediate difference. Figure 4.27 shows that the laminar model experiences a more significant immediate boundary effect but is able to reduce it to a steady state while the bulk model is not able to. Additionally,

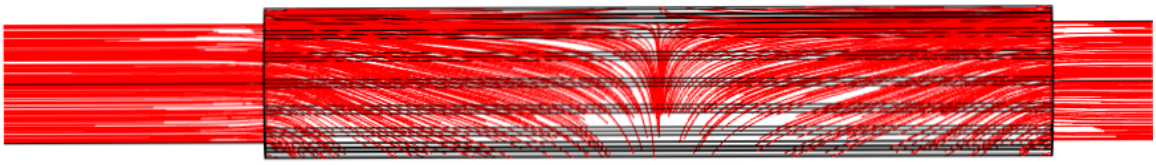

(a) Visualization of the displacement streamline in the bulk nerve model with a fully reinforced cuff.

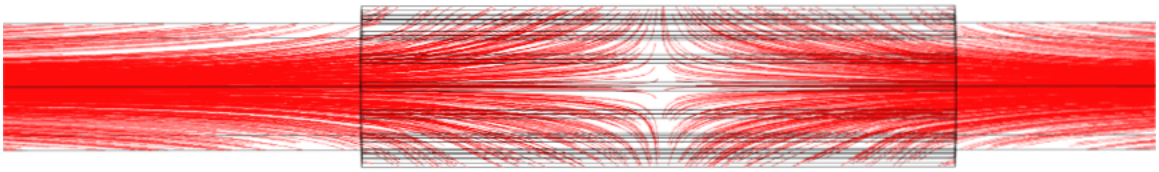

(b) Visualization of the displacement streamline in a laminar nerve model with a fully reinforced cuff.

Fig. 4.24.: Visualization of the displacement streamlines in the laminar and bulk nerve models with the full reinforced cuff to compare the effects of the nerve model on the strain reduction mechanism.

the difference between the surface variation and steady state is much greater in the laminar model than the bulk model. This would be likely from the epineurium's very low modulus value experience a more dramatic strain change compared to the bulk model.

The difference between models are the magnitude and shape of the boundary effects caused by the attachment of the cuff. These differences are caused by the perineurium layer preventing boundary transfer to the endoneurium from the epineurium, and the epineurium experiencing larger surface strain due to its lower stiffness. Further use of these models in designing different electrodes can give critical insight to how the electrodes may behave during chronic implantation.

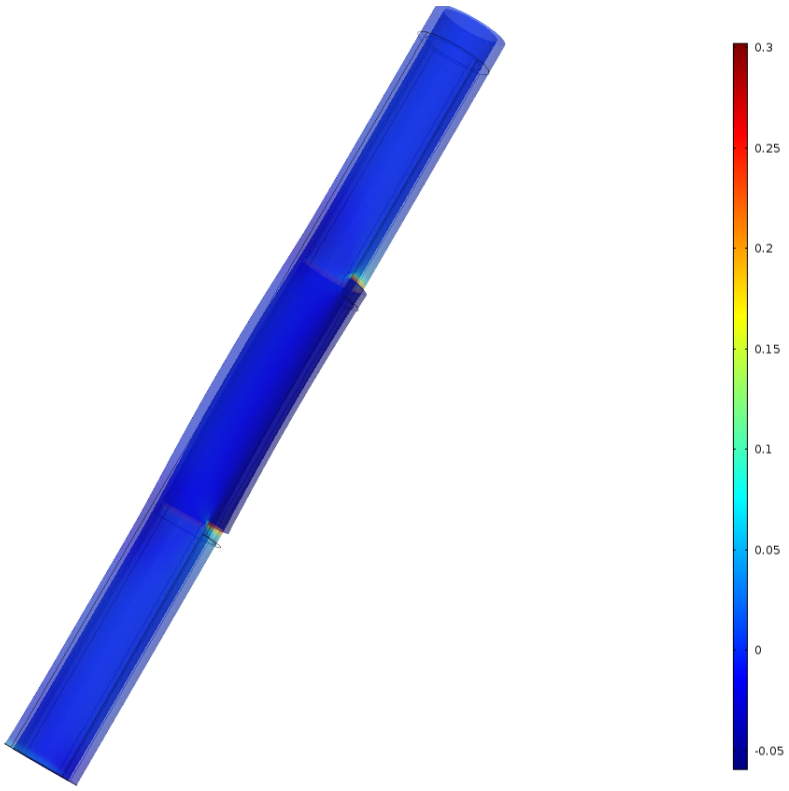

Fig. 4.25.: Results of the finite element analysis of the short laminar nerve with a half cuff in tension and plotted with a color map of axial strain.

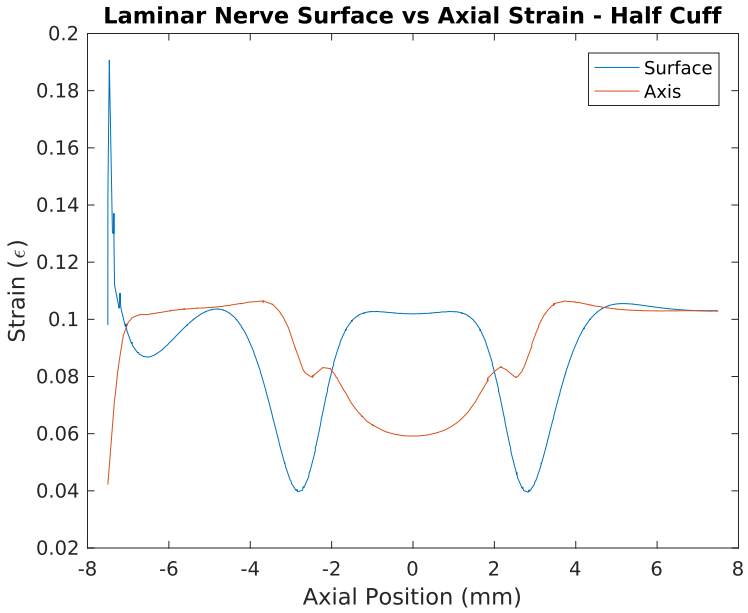

Fig. 4.26.: Comparison of the central axial strain and surface axial strain in the laminar models with a half cuff attached by plotting as a function of length.

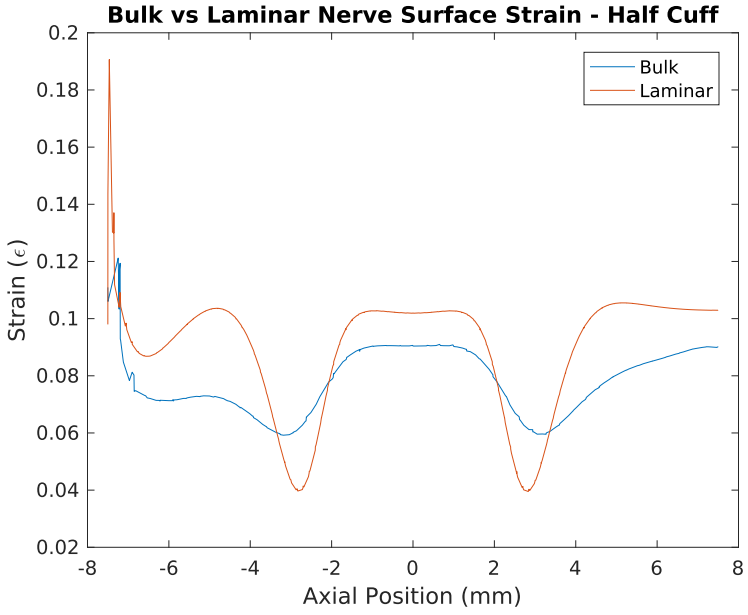

Fig. 4.27.: Comparison of the surface axial strain in the bulk and laminar models with a half cuff attached by plotting as a function of length of the nerve.

5. FUTURE DIRECTIONS

5.1 Summary of Outcomes

Using the techniques of finite element analysis, mechanical tensile testing, and imaging in nervous tissue deformation the present work addresses the characterization of the mechanical relationships between the nerve and the material properties of the electrode through the following specific aims:

1. Created and developed a histologically informed finite element model (FEM) to analyze the strain environment of a nerve and shape memory polymer (SMP) cuff electrode and predict strain patterns.

2. Demonstrated a reduction of strain in the nerve using ex-vivo tensile mechanical testing with shape memory polymer (SMP) cuff electrode attachment.

3. Demonstrated the location dependence of strain reduction in the nerve during ex-vivo tensile mechanical testing using digital image correlation techniques and FEA. Identified and proposed solutions for a potential mechanism that may drive chronic encapsulation in implantation.

The work of chapters 2 and 3 synthesize with the developed DIC in chapter 4 to create a simple and cost efficient predictive model for the strain variation environment. The identification of a potential mechanism for the continued chronic fibrotic encapsulation in chapter 4 and the proposal for potential new cuff designs to avoid this mechanism lead to many new questions that may be asked in future studies to continue the works explored in this thesis. Section 5.2 expands on this idea with potential avenues to explore.

5.2 Potential Future Studies

To further develop the work here, there are multiple avenues to explore that involve: cuff electrode manufacturing, biocompatibility in chronic studies, model improvement, and digital image correlation technique improvement.

Developing various cuffs and manufacturing them for different attachment purposes would serve to create an interesting study. The ends of the cuff's geometry could be changed to allow for various attachment methods and the coupling of this with finite element analysis could allow for significant progress in implantation methods.

The chronic biocompatibility of these cuffs should be testing through implantation and observation of fibrous encapsulation. In addition, cellular studies relating to mechanotransduction could be performed where intentionally stretched nerves are monitored and stained for cellular presence using immunohistochemistry techniques. This study would validate mechanisms theorized in this work and would help in understanding potential next steps for preventing encapsulation.

The finite element model can be continually improved through the adoption of multi-directional strain dependencies and non-linear strain energy density functions. Taking the next step in the finite element model to change from perfectly cylindrical to including various diameters of the nerve may also improve fidelity and model predictability.

Continuous improvement of the digital image correlation system is also possible. The simple ink transfer technique results in low spatial sampling, but through the use of quantum dots or high energy speckling, multi-dimensional analysis can be possible. In addition, the use of higher speed camera lens will allow for additional time analysis for higher sampling rates.

There are many directions to take the future work, much of it involving the improvement in predictability of finite element modeling techniques to realistic scenarios.

5.3 Contributions and Outcomes

The work in this thesis was funded and supported through Dr. Ken Yoshida's lab by the IUPUI Biomedical Engineering Department with a Graduate Research Assistantship and through an extended grant with GlaxoSmithKline.

The writing and research in chapter 2 contributed to the authoring of a chapter in the new edition of Neuroprosthetics: Theory and Practice. The histological work will also contribute to an article regarding impedance characteristics of the canine vagus nerve.

The work in chapters 2 and 3 will be combined and submitted as a paper to a journal such as the Journal for Biology, Engineering, and Medicine.

The work in chapter 4 will be developed into a paper and submitted to a journal such as the Journal for Biology, Engineering, and Medicine. It will also result in the creation of a new invention disclosure to the IU Research Technology Corporation. It will also support a new Spark grant proposal to the National Institute of Health in conjunction with support from GlaxoSmithKline and Google's joint venture into bioelectric medicine, Galvani Bioelectronics.

Projects outside of this work, supported by the IUPUI Biomedical Engineering Department and the IUPUI School of Engineering and Technology Student Council include my election to the position of President of the Biomedical Engineering Graduate Student Association and the Coordinator for Academic Success Initiatives with the ET Student Council. As the Coordinator for Academic Success Initiatives I received support from the Biomedical Engineering and Mechanical Engineering Departments to create programs for aiding student success in 200-level courses where I was awarded a $50,000 grant through the Office of the Dean of Engineering and Technology. This work is now supporting proposals to the National Science Foundation in conjunction with IUPUI's STEM Education Innovation and Research Institute.

LIST OF REFERENCES

LIST OF REFERENCES

[1] K. Ziegler-Graham, E. J. MacKenzie, P. L. Ephraim, T. G. Travison, and R. Brookmeyer, "Estimating the Prevalence of Limb Loss in the United States: 2005 to 2050," *Archives of Physical Medicine and Rehabilitation*, vol. 89, no. 3, pp. 422–429, Mar. 2008.

[2] S. Krahl, "Vagus nerve stimulation for epilepsy: A review of the peripheral mechanisms," *Surgical Neurology International*, vol. 3, no. 2, p. 47, 2012.

[3] M. Sahin and J. Huang, "Obstructive Sleep Apnea: Electrical Stimulation Treatment," in *Wiley Encyclopedia of Biomedical Engineering*. John Wiley & Sons, Inc., 2006.

[4] S. Micera, J. Carpaneto, and S. Raspopovic, "Control of hand prostheses using peripheral information," *Biomedical Engineering, IEEE Reviews in*, vol. 3, pp. 48–68, 2010.

[5] A. E. Schultz and T. A. Kuiken, "Neural interfaces for control of upper limb prostheses: the state of the art and future possibilities," *PM&R*, vol. 3, no. 1, pp. 55–67, 2011.

[6] Y. C. Fung, "What are the residual stresses doing in our blood vessels?" *Annals of biomedical engineering*, vol. 19, no. 3, pp. 237–249, 1991.

[7] M. A. Patestas and L. P. Gartner, *A Textbook of Neuroanatomy*, 1st ed. Malden, MA: Wiley-Blackwell, May 2006.

[8] D. Robertson, I. Biaggioni, G. Burnstock, P. A. Low, and J. F. R. Paton, Eds., *Primer on the Autonomic Nervous System, Third Edition*, 3rd ed. Amsterdam ; Boston: Academic Press, Nov. 2011.

[9] H.-R. Berthoud and W. L. Neuhuber, "Functional and chemical anatomy of the afferent vagal system," *Autonomic Neuroscience*, vol. 85, no. 13, pp. 1–17, Dec. 2000.

[10] B. M. Uthman, "Vagus nerve stimulation for seizures," *Archives of Medical Research*, vol. 31, no. 3, pp. 300–303, Jun. 2000.

[11] C. B. Nemeroff, H. S. Mayberg, S. E. Krahl, J. McNamara, A. Frazer, T. R. Henry, M. S. George, D. S. Charney, and S. K. Brannan, "VNS Therapy in Treatment-Resistant Depression: Clinical Evidence and Putative Neurobiological Mechanisms," *Neuropsychopharmacology*, vol. 31, no. 7, pp. 1345–1355, Apr. 2006.

[12] G. S. D. Dr and K. W. Horch, Eds., *Neuroprosthetics: Theory and Practice*. River Edge, NJ: World Scientific Publishing Company, Feb. 2004.

[13] W. B. Marks and G. E. Loeb, "Action currents, internodal potentials, and extracellular records of myelinated mammalian nerve fibers derived from node potentials," *Biophysical Journal*, vol. 16, no. 6, pp. 655–668, Jun. 1976.

[14] G. E. Loeb, M. J. Bak, M. Salcman, and E. M. Schmidt, "Parylene as a chronically stable, reproducible microelectrode insulator," *IEEE transactions on biomedical engineering*, vol. 24, no. 2, pp. 121–128, Mar. 1977.

[15] R. G. Hallin and G. Wu, "Protocol for microneurography with concentric needle electrodes," *Brain Research. Brain Research Protocols*, vol. 2, no. 2, pp. 120–132, Jan. 1998.

[16] C. Gonzlez and M. Rodrguez, "A flexible perforated microelectrode array probe for action potential recording in nerve and muscle tissues," *Journal of Neuroscience Methods*, vol. 72, no. 2, pp. 189–195, Apr. 1997.

[17] B. L. McNaughton, J. O'Keefe, and C. A. Barnes, "The stereotrode: a new technique for simultaneous isolation of several single units in the central nervous system from multiple unit records," *Journal of Neuroscience Methods*, vol. 8, no. 4, pp. 391–397, Aug. 1983.

[18] A. Branner, R. B. Stein, and R. A. Normann, "Selective stimulation of cat sciatic nerve using an array of varying-length microelectrodes," *Journal of Neurophysiology*, vol. 85, no. 4, pp. 1585–1594, Apr. 2001.

[19] A. Branner and R. A. Normann, "A multielectrode array for intrafascicular recording and stimulation in sciatic nerve of cats," *Brain Research Bulletin*, vol. 51, no. 4, pp. 293–306, Mar. 2000.

[20] V. K. Mushahwar, D. F. Collins, and A. Prochazka, "Spinal cord microstimulation generates functional limb movements in chronically implanted cats," *Experimental Neurology*, vol. 163, no. 2, pp. 422–429, Jun. 2000.

[21] K. R. Harreby, A. Kundu, K. Yoshida, T. Boretius, T. Stieglitz, and W. Jensen, "Subchronic Stimulation Performance of Transverse Intrafascicular Multichannel Electrodes in the Median Nerve of the Gttingen Minipig: Transverse Intrafascicular Multichannel Electrodes," *Artificial Organs*, vol. 39, no. 2, pp. E36–E48, Feb. 2015.

[22] C. M. Gray, P. E. Maldonado, M. Wilson, and B. McNaughton, "Tetrodes markedly improve the reliability and yield of multiple single-unit isolation from multi-unit recordings in cat striate cortex," *Journal of Neuroscience Methods*, vol. 63, no. 1-2, pp. 43–54, Dec. 1995.

[23] B. R. Bowman and R. C. Erickson, "Acute and chronic implantation of coiled wire intraneural electrodes during cyclical electrical stimulation," *Annals of Biomedical Engineering*, vol. 13, no. 1, pp. 75–93, 1985.

[24] M. S. Malagodi, D. K. W. Horch, and A. A. Schoenberg, "An intrafascicular electrode for recording of action potentials in peripheral nerves," *Annals of Biomedical Engineering*, vol. 17, no. 4, pp. 397–410, Jul. 1989.

[25] N. Nannini and K. Horch, "Muscle recruitment with intrafascicular electrodes," *IEEE transactions on bio-medical engineering*, vol. 38, no. 8, pp. 769–776, Aug. 1991.

[26] K. Yoshida and K. Horch, "Reduced fatigue in electrically stimulated muscle using dual channel intrafascicular electrodes with interleaved stimulation," *Annals of Biomedical Engineering*, vol. 21, no. 6, pp. 709–714, Dec. 1993.

[27] K. Yoshida, D. Pellinen, D. Pivin, P. Rousche, and D. Kipke, "Development of the thin-film longitudinal intra-fascicular electrode," 2000.

[28] K. Kallese, *Implantable Transducers for Neurokinesiological Research and Neural Prostheses [microform]*. Thesis (Ph.D.)–Simon Fraser University, 1998.

[29] S. Muceli, F. Negro, W. Jensen, K. Yoshida, W. Poppendieck, T. Doerge, and D. Farina, "Sampling large populations of motor units in humans with multichannel thin-film electrodes," 2010.

[30] A. Cutrone, J. Del Valle, D. Santos, J. Badia, C. Filippeschi, S. Micera, X. Navarro, and S. Bossi, "A three-dimensional self-opening intraneural peripheral interface (SELINE)," *Journal of Neural Engineering*, vol. 12, no. 1, p. 016016, Feb. 2015.

[31] R. B. Stein, T. R. Nichols, J. Jhamandas, L. Davis, and D. Charles, "Stable long-term recordings from cat peripheral nerves," *Brain Research*, vol. 128, no. 1, pp. 21–38, Jun. 1977.

[32] R. B. Stein, D. Charles, T. Gordon, J. A. Hoffer, and J. Jhamandas, "Impedance properties of metal electrodes for chronic recording from mammalian nerves," *IEEE transactions on bio-medical engineering*, vol. 25, no. 6, pp. 532–537, Nov. 1978.

[33] L. N. Andreasen, J. J. Struijk, and S. Lawrence, "Measurement of the performance of nerve cuff electrodes for recording," *Medical & Biological Engineering & Computing*, vol. 38, no. 4, pp. 447–453, Jul. 2000.

[34] M. Sahin, M. A. Haxhiu, D. M. Durand, and I. A. Dreshaj, "Spiral nerve cuff electrode for recordings of respiratory output," *Journal of Applied Physiology (Bethesda, Md.: 1985)*, vol. 83, no. 1, pp. 317–322, Jul. 1997.

[35] G. G. Naples, J. T. Mortimer, A. Scheiner, and J. D. Sweeney, "A spiral nerve cuff electrode for peripheral nerve stimulation," *IEEE transactions on bio-medical engineering*, vol. 35, no. 11, pp. 905–916, Nov. 1988.

[36] J. O. Larsen, M. Thomsen, M. Haugland, and T. Sinkjaer, "Degeneration and regeneration in rabbit peripheral nerve with long-term nerve cuff electrode implant: a stereological study of myelinated and unmyelinated axons," *Acta Neuropathologica*, vol. 96, no. 4, pp. 365–378, Oct. 1998.

[37] T. E. Milner and J. A. Hoffer, "Long-term peripheral nerve and muscle recordings from normal and dystrophic mice," *Journal of Neuroscience Methods*, vol. 19, no. 1, pp. 37–45, Jan. 1987.

[38] C. Veraart, W. M. Grill, and J. T. Mortimer, "Selective control of muscle activation with a multipolar nerve cuff electrode," *IEEE transactions on bio-medical engineering*, vol. 40, no. 7, pp. 640–653, Jul. 1993.

[39] Schuettler and T. Stieglitz, "18polar Hybrid Cuff Electrodes for Stimulation of Peripheral Nerves," 2000.

[40] D. J. Tyler and D. M. Durand, "A slowly penetrating interfascicular nerve electrode for selective activation of peripheral nerves," *IEEE transactions on rehabilitation engineering: a publication of the IEEE Engineering in Medicine and Biology Society*, vol. 5, no. 1, pp. 51–61, Mar. 1997.

[41] D. Tyler and D. M. Durand, "Alteration of neural geometry for selective nerve stimulation," in *Proceedings of the 19th Annual International Conference of the IEEE Engineering in Medicine and Biology Society, 1997*, vol. 5, 1997, pp. 2002–2003 vol.5.

[42] M. A. Schiefer, K. H. Polasek, R. J. Triolo, G. C. J. Pinault, and D. J. Tyler, "Selective stimulation of the human femoral nerve with a flat interface nerve electrode," *Journal of Neural Engineering*, vol. 7, no. 2, p. 26006, Apr. 2010.

[43] H. Helmholtz, "Ueber einige Gesetze der Vertheilung elektrischer Strome in korperlichen Leitern mit Anwendung auf die thierisch-elektrischen Versuche," *Ann Physik und Chemie*, vol. 89, pp. 211–33,354–77, 1853.

[44] J. Malmivuo and R. Plonsey, *Bioelectromagnetism - Principles and Applications of Bioelectric and Biomagnetic Fields*, Jan. 1995.

[45] O. H. Schmitt, "Lead vectors and transfer impedance," *Annals of the New York Academy of Sciences*, vol. 65, no. 6, pp. 1092–1109, Aug. 1957.

[46] S. Grimnes and O. G. Martinsen, *Bioimpedance and Bioelectricity Basics, Third Edition*, 3rd ed. Boston, MA: Academic Press, Sep. 2014.

[47] E. Zheng, S. Shao, and J. G. Webster, "Impedance of skeletal muscle from 1 Hz to 1 MHz," *IEEE transactions on bio-medical engineering*, vol. 31, no. 6, pp. 477–481, Jun. 1984.

[48] W. M. Grill and J. T. Mortimer, "Electrical properties of implant encapsulation tissue," *Annals of Biomedical Engineering*, vol. 22, no. 1, pp. 23–33, Feb. 1994.

[49] H. P. Schwan, "Electrode polarization impedance and measurements in biological materials," *Annals of the New York Academy of Sciences*, vol. 148, no. 1, pp. 191–209, Feb. 1968.

[50] R. Lorente de No, "Analysis of the distribution of the action currents of nerve in volume conductors," *Studies from the Rockefeller Institute for Medical Research. Reprints. Rockefeller Institute for Medical Research*, vol. 132, pp. 384–477, 1947.

[51] P. Rosenfalck, "Intra- and extracellular potential fields of active nerve and muscle fibres. A physico-mathematical analysis of different models," *Acta Physiologica Scandinavica. Supplementum*, vol. 321, pp. 1–168, 1969.

[52] R. Plonsey, "Action potential sources and their volume conductor fields," *Proceedings of the IEEE*, vol. 65, no. 5, pp. 601–611, May 1977.

[53] R. Schoonhoven and D. F. Stegeman, "Models and analysis of compound nerve action potentials," *Critical Reviews in Biomedical Engineering*, vol. 19, no. 1, pp. 47–111, 1991.

[54] J. Clark and R. Plonsey, "The extracellular potential field of the single active nerve fiber in a volume conductor," *Biophysical Journal*, vol. 8, no. 7, pp. 842–864, Jul. 1968.

[55] D. F. Stegeman, J. P. de Weerd, and E. G. Eijkman, "A volume conductor study of compound action potentials of nerves in situ: the forward problem," *Biological Cybernetics*, vol. 33, no. 2, pp. 97–111, Jun. 1979.

[56] R. Schoonhoven, D. F. Stegeman, and J. P. de Weerd, "The forward problem in electroneurography. I: A generalized volume conductor model," *IEEE transactions on bio-medical engineering*, vol. 33, no. 3, pp. 327–334, Mar. 1986.

[57] N. Ganapathy and J. W. Clark, "Extracellular currents and potentials of the active myelinated nerve fiber," *Biophysical Journal*, vol. 52, no. 5, pp. 749–761, Nov. 1987.

[58] R. Plonsey, "The active fiber in a volume conductor," *IEEE transactions on bio-medical engineering*, vol. 21, no. 5, pp. 371–381, Sep. 1974.

[59] P. Rabischong, F. Bonnel, E. Dombre, E. Peruchon, P. Coiffet, B. Fournier, and J. M. Brebic, "Electrical stimulation of limbs." *Bulletin of prosthetics research*, pp. 261–290, 1973.

[60] D. R. McNeal, L. L. Baker, and J. T. Symons, "Recruitment data for nerve cuff electrodes: implications for design of implantable stimulators," *IEEE Transactions on Biomedical Engineering*, vol. 36, no. 3, pp. 301–308, Mar. 1989.

[61] K. H. Polasek, H. A. Hoyen, M. W. Keith, R. F. Kirsch, and D. J. Tyler, "Spiral Nerve Cuff Electrodes for an Upper Extremity Neuroprosthesis," in *2006 International Conference of the IEEE Engineering in Medicine and Biology Society*, Aug. 2006, pp. 3584–3587.

[62] R. Jung, K. Ichihara, G. Venkatasubramanian, and J. J. Abbas, "Chronic Neuromuscular Electrical Stimulation of Paralyzed Hindlimbs in a Rodent Model," *Journal of neuroscience methods*, vol. 183, no. 2, pp. 241–254, Oct. 2009.

[63] T. Boretius, J. Badia, A. Pascual-Font, M. Schuettler, X. Navarro, K. Yoshida, and T. Stieglitz, "A transverse intrafascicular multichannel electrode (TIME) to interface with the peripheral nerve," *Biosensors & Bioelectronics*, vol. 26, no. 1, pp. 62–69, Sep. 2010.

[64] A. Branner, R. B. Stein, E. Fernandez, Y. Aoyagi, and R. A. Normann, "Long-term stimulation and recording with a penetrating microelectrode array in cat sciatic nerve," *IEEE transactions on bio-medical engineering*, vol. 51, no. 1, pp. 146–157, Jan. 2004.

[65] J. Badia, T. Boretius, A. Pascual-Font, E. Udina, T. Stieglitz, and X. Navarro, "Biocompatibility of chronically implanted transverse intrafascicular multichannel electrode (TIME) in the rat sciatic nerve," *IEEE transactions on bio-medical engineering*, vol. 58, no. 8, Aug. 2011.

[66] N. Lago, K. Yoshida, K. P. Koch, and X. Navarro, "Assessment of biocompatibility of chronically implanted polyimide and platinum intrafascicular electrodes," *IEEE transactions on bio-medical engineering*, vol. 54, no. 2, pp. 281–290, Feb. 2007.

[67] K. Polasek, H. Hoyen, M. Keith, R. Kirsch, and D. Tyler, "Stimulation Stability and Selectivity of Chronically Implanted Multicontact Nerve Cuff Electrodes in the Human Upper Extremity," *IEEE Transactions on Neural Systems and Rehabilitation Engineering*, vol. 17, no. 5, pp. 428–437, Oct. 2009.

[68] S. Qiao, "Bioelectric Nerve Fiber to Electrode Coupling for Unit Identification and Tracking," PhD. Dissertation, Purdue University, West Lafayette, Indiana, Aug. 2014.

[69] M. Horn, "A Nerve Fiber Model and Prediction of Electrode-Fiber Coupling Simulation for Design of Peripheral Nerve Interfaces," Master's Thesis, Indiana University Purdue University Indianapolis, Indianapolis, IN, USA, Sep. 2016.

[70] V. S. Polikov, P. A. Tresco, and W. M. Reichert, "Response of brain tissue to chronically implanted neural electrodes," *Journal of Neuroscience Methods*, vol. 148, no. 1, pp. 1–18, Oct. 2005.

[71] J. Thelin, H. Jrntell, E. Psouni, M. Garwicz, J. Schouenborg, N. Danielsen, and C. E. Linsmeier, "Implant Size and Fixation Mode Strongly Influence Tissue Reactions in the CNS," *PLoS ONE*, vol. 6, no. 1, Jan. 2011.

[72] W. M. Grill and J. T. Mortimer, "Neural and connective tissue response to long-term implantation of multiple contact nerve cuff electrodes," *Journal of Biomedical Materials Research*, vol. 50, no. 2, pp. 215–226, May 2000. [Online]. Available: http://onlinelibrary.wiley.com.proxy.ulib.uits.iu.edu/doi/10.1002/(SICI)1097-4636(200005)50:2⟨215::AID-JBM17⟩3.0.CO;2-A/abstract

[73] J. N. Reddy, *An Introduction to the Finite Element Method*, 3rd ed. McGraw-Hill Education / Asia, May 2005.

[74] M. Kazemi, Y. Dabiri, and L. P. Li, "Recent Advances in Computational Mechanics of the Human Knee Joint," *Computational and Mathematical Methods in Medicine*, vol. 2013, 2013.

[75] S. Chokhandre, J. P. Halloran, A. J. van den Bogert, and A. Erdemir, "A Three-Dimensional Inverse Finite Element Analysis of the Heel Pad," *Journal of Biomechanical Engineering*, vol. 134, no. 3, pp. 31 002–NaN, Mar. 2012.

[76] H.-Y. Lee, S.-J. Kim, K.-T. Kang, S.-H. Kim, and K.-K. Park, "The Effect of Tibial Posterior Slope on Contact Force and Ligaments Stresses in Posterior-Stabilized Total Knee Arthroplasty-Explicit Finite Element Analysis," *Knee Surgery & Related Research*, vol. 24, no. 2, pp. 91–98, Jun. 2012.

[77] L. C. Fitton, J. F. Shi, M. J. Fagan, and P. OHiggins, "Masticatory loadings and cranial deformation in Macaca fascicularis: a finite element analysis sensitivity study," *Journal of Anatomy*, vol. 221, no. 1, pp. 55–68, Jul. 2012.

[78] D. W. Park, M. S. Richards, J. M. Rubin, J. Hamilton, G. H. Kruger, and W. F. Weitzel, "Arterial elasticity imaging: comparison of finite-element analysis models with high-resolution ultrasound speckle tracking," *Cardiovascular Ultrasound*, vol. 8, p. 22, Jun. 2010.

[79] G. Krishnamurthy, D. B. Ennis, A. Itoh, W. Bothe, J. C. Swanson, M. Karlsson, E. Kuhl, D. C. Miller, and N. B. Ingels, "Material properties of the ovine mitral valve anterior leaflet in vivo from inverse finite element analysis," *American Journal of Physiology - Heart and Circulatory Physiology*, vol. 295, no. 3, pp. H1141–H1149, Sep. 2008.

[80] Y. C. Fung, "Elasticity of soft tissues in simple elongation," *American Journal of PhysiologyLegacy Content*, vol. 213, no. 6, pp. 1532–1544, 1967.

[81] Y. Fung, *Biomechanics: mechanical properties of living tissues*, 2nd ed. New York: Springer-Verlag, 1993.

[82] C. J. Chuong and Y. C. Fung, "On residual stresses in arteries," *Journal of Biomechanical Engineering*, vol. 108, no. 2, pp. 189–192, May 1986.

[83] J. H. Omens and Y. C. Fung, "Residual strain in rat left ventricle," *Circulation Research*, vol. 66, no. 1, pp. 37–45, Jan. 1990.

[84] H. C. Han and Y. C. Fung, "Residual strains in porcine and canine trachea," *Journal of Biomechanics*, vol. 24, no. 5, pp. 307–315, 1991.

[85] H. Gregersen, G. S. Kassab, and Y. C. Fung, "The zero-stress state of the gastrointestinal tract: biomechanical and functional implications," *Digestive Diseases and Sciences*, vol. 45, no. 12, pp. 2271–2281, Dec. 2000.

[86] D. R. Carter, D. P. Fyhrie, and R. T. Whalen, "Trabecular bone density and loading history: regulation of connective tissue biology by mechanical energy," *Journal of Biomechanics*, vol. 20, no. 8, pp. 785–794, 1987.

[87] J. Wolff, "Uber die innere Architektur der Knochen und ihre Bedeutung ffir die Frage vom Knochen- wachstum." *Archiv f/ir pathologische Anatomie und Physiologie und fiir Klinische Medizin (Virchows Archiv)*, vol. 50, pp. 389–453, 1870.

[88] B. Zhou, S. Ravindran, J. Ferdous, A. Kidane, M. A. Sutton, and T. Shazly, "Using Digital Image Correlation to Characterize Local Strains on Vascular Tissue Specimens," *JoVE (Journal of Visualized Experiments)*, no. 107, pp. e53 625–e53 625, Jan. 2016.

[89] M. S. Thompson, H. Schell, J. Lienau, and G. N. Duda, "Digital image correlation: a technique for determining local mechanical conditions within early bone callus," *Medical Engineering & Physics*, vol. 29, no. 7, pp. 820–823, Sep. 2007.

[90] T. C. Doehring, M. Kahelin, and I. Vesely, "Direct Measurement of Nonuniform Large Deformations in Soft Tissues During Uniaxial Extension," *Journal of Biomechanical Engineering*, vol. 131, no. 6, p. 061001, 2009.

[91] T. Ware, D. Simon, K. Hearon, C. Liu, S. Shah, J. Reeder, N. Khodaparast, M. P. Kilgard, D. J. Maitland, R. L. Rennaker, and W. E. Voit, "Three-Dimensional Flexible Electronics Enabled by Shape Memory Polymer Substrates for Responsive Neural Interfaces," *Macromolecular Materials and Engineering*, vol. 297, no. 12, pp. 1193–1202, Dec. 2012.

[92] T. Ware, D. Simon, C. Liu, T. Musa, S. Vasudevan, A. Sloan, E. W. Keefer, R. L. Rennaker, and W. Voit, "Thiol-ene/acrylate substrates for softening intracortical electrodes: Substrates for intracortical electrodes," *Journal of Biomedical Materials Research Part B: Applied Biomaterials*, vol. 102, no. 1, pp. 1–11, Jan. 2014.

[93] S. S. Sunderland, *Nerves And Nerve Injuries*. Churchill Livingstone, 1978.

[94] S. Sunderland, "The connective tissues of peripheral nerves," *Brain: A Journal of Neurology*, vol. 88, no. 4, pp. 841–854, Nov. 1965.

[95] G. H. Borschel, K. F. Kia, W. M. Kuzon Jr, and R. G. Dennis, "Mechanical properties of acellular peripheral nerve," *Journal of Surgical Research*, vol. 114, no. 2, pp. 133–139, Oct. 2003.

[96] J. A. Beel, D. E. Groswald, and M. W. Luttges, "Alterations in the mechanical properties of peripheral nerve following crush injury," *Journal of Biomechanics*, vol. 17, no. 3, pp. 185–193, 1984.

[97] F. P. Beer, E. R. J. Jr, J. T. DeWolf, and D. F. Mazurek, *Mechanics of Materials, 7th Edition*, 7th ed. New York, NY: McGraw-Hill Education, Jan. 2014.

[98] Winnie Jensen, K. Yoshida, and U. Hofmann, "In-vivo implant mechanics of flexible, silicon-based ACREO microelectrode arrays in rat cerebral cortex," *IEEE Trans Biomed Eng.*, vol. 53, no. 5, pp. 934–940, May 2006. [Online]. Available: http://ieeexplore.ieee.org/xpl/articleDetails.jsp?arnumber=1621145

[99] E. Clarke and J. G. Bearn, "The spiral nerve bands of Fontana," *Brain: A Journal of Neurology*, vol. 95, no. 1, pp. 1–20, 1972.

[100] R. O. Duda and P. E. Hart, "Use of the Hough Transformation to Detect Lines and Curves in Pictures," *Commun. ACM*, vol. 15, no. 1, pp. 11–15, Jan. 1972.

[101] L. G. Shapiro and G. C. Stockman, *Computer Vision*, 1st ed. Upper Saddle River, NJ: Pearson, Feb. 2001.

[102] T. R. Singh, S. Roy, O. I. Singh, T. Sinam, and K. M. Singh, "A New Local Adaptive Thresholding Technique in Binarization," *arXiv:1201.5227 [cs]*, Jan. 2012, arXiv: 1201.5227.

[103] W. Gao, X. Zhang, L. Yang, and H. Liu, "An improved Sobel edge detection," in *2010 3rd International Conference on Computer Science and Information Technology*, vol. 5, Jul. 2010, pp. 67–71.

[104] M. R. K. Mofrad and R. D. Kamm, Eds., *Cellular Mechanotransduction: Diverse Perspectives from Molecules to Tissues*, 1st ed. Cambridge ; New York: Cambridge University Press, Nov. 2009.

[105] H. G. Leach, I. Chrobak, R. Han, and M. Trojanowska, "Endothelial Cells Recruit Macrophages and Contribute to a Fibrotic Milieu in Bleomycin Lung Injury," *American Journal of Respiratory Cell and Molecular Biology*, vol. 49, no. 6, pp. 1093–1101, Dec. 2013.